# **Geostrophic circulation and tidal effects in the Gulf of Gabès**

- 2 Maher Bouzaiene<sup>1</sup>, Antonio Guarnieri<sup>1</sup>, Damiano Delrosso<sup>1</sup>, Ahmad F. Dilmahamod<sup>2</sup>, Simona
- 3 Simoncelli<sup>1</sup>, Claudia Fratianni<sup>1</sup>
- <sup>1</sup>Istituto Nazionale di Geofisica e Vulcanologia, Sezione di Bologna, Viale Berti Pichat 6/2, 40127, Bologna, Italy
- <sup>2</sup>GEOMAR Helmholtz Centre for Ocean Research Kiel, Wischhofstr 1-3, 24148 Kiel, Germany
- 6 Correspondence to: Maher Bouzaiene (maher.bouzaiene@ingv.it)
- 7 **Abstract.** The mean kinematic features in the Gulf of Gabès region is analyzed based on 30 years of altimetry data (1993-
- 8 2022) and the outputs of a high resolution ocean model for the year 2022. A comparison of the seasonal variability in three
- 9 different geographical areas within the gulf is presented. In the northern and southern parts of the gulf, anticyclonic
- 10 structures prevail, while the central area is dominated by divergence. Similarity in the flow topology is found in these three
- areas of the gulf due to the signature of hyperbolic regions. In winter and fall, the mean flow is oriented northward while it is
- 12 reversed in spring and summer. The tidal perturbation influences sea level, kinetic energy and hyperbolic geostrophic
- structures, leading to the generation of a cyclonic current located in the central part of the gulf and to the presence of
- 14 persistent strain gradients amplifying hyperbolic structures. The Finite Time Lyapunov Exponent (FTLE) computed using
- 15 altimetry data highlights the link between physical and biogeochemical processes, with the Gulf of Gabès mean circulation
- 16 features acting as transport barriers for phytoplankton dispersion.

#### 1 Introduction

- Tidal forcing plays a crucial role in ocean circulation, and the Gulf of Gabès (GG) is notably influenced by this phenomenon.
- 19 Understanding tidal interactions with complex dynamics and their impact on the transport of passive and active tracers
- 20 (such as pollutants and marine species) is challenging (Meyerjürgens et al, 2020). Well-known as a region of relevant tides
- within the Mediterranean Sea (Abdennadher and Boukthir, 2006) with a semi-arid climate, high temperature, relatively high
- 22 salinity and strong density gradients, the GG is located in the southern part of the Sicily Channel and represents a site of
- water masses exchange between the western and the eastern Mediterranean Sea basins.
- 24 The gulf is considered one of the richest areas of the Mediterranean Sea in terms of nutrients availability and biological
- production (Salgado-Hernanz et al, 2019). Due to the gentle slope of its continental shelf and its shallow depth (Figure 1),
- the GG has the highest tidal range (with difference between high and low tide up to almost 2 m) in the Mediterranean Sea, is
- 27 one of the areas in the Mediterranean Sea where the highest tides can be found (Othmani et al., 2017) which strongly
- 28 influences its circulation (Abdennadher and Boukthir, 2006; Sammari et al., 2006; Poulain and Zambianchi, 2007). Apart
- 29 from the tides, anticyclonic winds are also one of the drivers of the GG circulation (Sammari et al., 2006). Originated from

the Atlantic Water (AW), the Atlantic Tunisian Current (ATC) and the Bifurcation Atlantic Tunisian Current (BATC) are the strongest surface currents evolving in the gulf (Ben Ismail et al., 2015), while the Atlantic Ionian Stream (AIS) is generated by current instability and topography (Menna et al., 2019), and it flows North of Malta island without penetrating in the GG (Figure 2a) (Pinardi et al., 2015; Bouzaiene et al., 2020). The ATC is a permanent surface current characterized by low salinity (Sammari et al., 1999). It crosses the Strait of Sicily and circulates along the Tunisian coast (Sorgente et al., 2011) where it splits into two branches. One of them interests the coastal strip and is directed southward (Ben Ismail et al., 2010). Due to its lower salinity, ATC branch circulates further offshore from the coast in a south-eastern direction where it eventually follows the Libyan plateau (Figure 2a) (Millot and TaupierLetage, 2005). This branch, observed especially in winter, is called the Atlantic Libyan Current (ALC). It circulates along the Libyan shelf break where the mean flow is represented by a weak current bounded by a cyclonic vortex referenced as the Libyan Shelf Break Vortex (LSBV, Sorgente et al., 2011, see Figure 2a). The BATC continues to circulate offshore, generating the Medina Gyre (MG) and the Southern Medina Gyre (SMG) (Figure 2a), whose formation is due to current instability or/and topography (Jouini et al., 2016, Menna et al., 2019).

The GG dynamics is characterized by small and large-scale inter-annual and seasonal variability in the surface layer (Jebri et al., 2016). This system is identified by many spatial-temporal structures interacting with each other and producing an extremely complex and variable circulation. Currents, filaments and eddies are responsible for water mass transport, thus the understanding of their seasonal and inter-annual variability is crucial for a wide variety of reasons, such as regional water exchanges with the open sea, large scale turbulent flow spreading, propagation of particles and dispersion of sediments in the coastal zones. This is even more important in the GG environment where the anthropogenic pressure has dramatically increased due to coastal phosphate processing plants by-products, frequent oil spill episodes, general pollution factors such as floating marine debris or plastic, micro and macro litter (Ben Ismail et al., 2022). In addition, Lagrangian studies on the transport of nutrients, jellyfish, eggs, and larvae would benefit from a better knowledge of the mean circulation variability. To provide a realistic study for the GG circulation it is necessary to evaluate in detail the long-term variability and the influence that tidal forcing, interacting with topography, exert on the system, resulting in the generation of new structures influencing turbulence and circulation in the entire gulf.

It has been shown in Elhmaidi et al. (1993) that turbulent features induce discrepancy between modeled and theoretical dispersion laws in case of two-dimensional turbulent dispersion theory for isotropic and homogeneous flow. Two anomalous absolute dispersion (5/3, elliptic) and (5/4, hyperbolic) power laws were found in previous studies (Bouzaiene et al., 2021). These anomalous regimes have been related to the sea topology through the presence of elliptic and hyperbolic structures (Bouzaiene et al., 2018, 2021). In the eddy inner parts, these areas are referred to as elliptic regions characterized by high vorticity gradients, while hyperbolic features are detected in the coherent structure outer parts and can be related to sheared/stretched ocean flow. In Gomez-Navarro et al, (2024) the impact of tidal forcing on surface particle transport is explored, while how tidal perturbation influences the dispersion of elliptic and hyperbolic regions lacks, in our opinion, a

certain degree of discussion.

- To our knowledge, the impact of tides on topology (the distribution of elliptic and hyperbolic regions) in the GG has not been studied before, even though tidal forcing is very important in this area. Hence, given their potential influence on phytoplankton blooms, nutrient distribution, and marine litter dispersion, it is essential to gain a better understanding of how tides influence the circulation, dynamics, and sea topology. Altimetry data analysis allows analyzing the geostrophic circulation and the kinematic properties of mesoscale structures. However, their low temporal and spatial resolutions do not allow performing a realistic study on the dynamics introduced by tides. In order to address this issue, we leveraged high temporal resolution (hourly) model outputs from a numerical system which includes tides.
- In this study, we focus on the kinematic properties of the geostrophic component of the circulation in the GG and on how tides affect currents. We do this by using altimetry data covering the time period 1993-2022 and model analysis data for the year 2022, both distributed by the Copernicus Marine Service (CMS, http://marine.copernicus.eu/). Previously, some efforts to understand this oceanographic system have been made by focusing on the general aspects of the Gulf of Gabès circulation (Ben Ismailet al. 2015, 2020; Zayen et al. 2020). The impact of internal waves on mesoscale eddies is studied in Barkan et
- al., (2017, 2021) where signal increases significantly when tidal forcing is present. Furthermore, the velocity fields from a high-resolution coupled ocean—wave model simulation (Clementi et al, 2021) impact simulated surface particle dispersal was
- studied in the mediterranean Sea (Rühs et al, 2025). The comprehension of how tides influence the geostrophic features is
- still an open question.

65

66

67

68

69

70

- 80 Our aim is to investigate new features of the geostrophic circulation, to assess the impact of tides on the geostrophic
- 81 circulation. High resolution ocean circulation modeling and satellite altimetry could enhance our understanding of the
- 82 geostrophic transport. The paper is organized as follows: in section 2 we describe the datasets used and the methods applied.
- The results on geostrophic structures from altimetry and model data are presented in section 3. Summary and conclusions
- are proposed in section 4.

#### 2 Material and methods

86 **2.1 Datasets** 

- 87 The geostrophic circulation in the GG has been investigated by means of remote-sensed altimetry data and outputs from a
- 88 high resolution oceanographic numerical system.
- 89 2.1.1 Altimetry data
- 90 The satellite altimetry dataset used in this study is a subset of the CMS SEALEVEL EUR PHY L4 MY 008 068 product
- 91 (European Union-Copernicus Marine Service. (2021), Mercator Ocean International, https://doi.org/10.48670/MOI-00141),
- with a spatial resolution of  $0.125^{\circ} \times 0.125^{\circ}$  and a daily temporal resolution. Our analyses were conducted over a 30-year
- 93 period, from 1993 to 2022. For more details see the Quality Information Document (QUID)
- 94 (https://documentation.marine.copernicus.eu/QUID/CMEMS-SL-QUID-008-032-068.pdf). The variable used is the absolute
- 95 surface geostrophic velocity and we inferred the vorticity, the divergence, the Okubo-Weiss parameter, the deformation

- 96 gradients and the Finite Time Lyapunov Exponent (FTLE) from the surface geostrophic velocity variable from the ADT.
- 97 These parameters were investigated in order to elucidate the mean circulation, persistent currents, eddies and gyres.

## 98 2.1.2 Chlorophyll-a data

- 99 The chlorophyll-a dataset used in this study is the CMS OCEANCOLOUR\_MED\_BGC\_L4\_MY\_009\_144 product. We
- 100 used the daily mass concentration of chlorophyll-a in sea water (CHL) at 1 km resolution from the Ocean Satellite
- Observations for multi-years Bio-Geo\_Chemical (BGC) regional datasets (https://doi.org/10.48670/moi-00300).

# 102 **2.1.3 Model data**

- Hourly Sea Surface Height (SSH) fields from model data (CMS MEDSEA ANALYSISFORECAST PHY 006 013
- (Clementi et al., 2021) covering the year 2022, are used to compute geostrophic currents. We have chosen the year 2022
- since at the time the dataset was processed it was the only complete year for the CMS system including tidal signal in the
- 106 hydrodynamic model used. The physical component of the Mediterranean Sea within the framework of CMS (Med-Physics)
- 107 is a tidal, coupled hydrodynamic-wave model with a data assimilation system implemented over the whole Mediterranean
- Sea, and a horizontal resolution of 1/24° (~4 km) and 141 unevenly spaced vertical z\* levels (Clementi et al. 2017). More
- 109 detailed information on the system and its products can be found in the Quality Information Document
- 110 (https://catalogue.marine.copernicus.eu/documents/QUID/CMEMS-MED-QUID-006-013.pdf).

# 111 **2.2 Methods**

- To describe the kinematic properties and the circulation of the GG we estimate the geostrophic currents for the year 2022
- from the model data (MEDSEA ANALYSISFORECAST PHY 006 013) SSH fields and we then compute the four
- following quantities from the altimetry data and model data (described in section 2.1.1 and 2.1.3, respectively): normalized
- vorticity (with respect to f), normalized divergence, normalized Okubo-Weiss parameter and FTLE.

# 116 **2.2.1** Estimation of the geostrophic currents

- The model SSH field (section 2.1.3) was used to estimate the geostrophic currents, resulting from the balance between the
- 118 Coriolis force and the horizontal pressure gradient. The zonal (ugeos) and the meridional (vgeos) components of the
- geostrophic velocities are derived from the geostrophic equations as follows (Apel, 1987; Vigo et al., 2018a; 2018b):

$$ugeos = \frac{-g}{f} \partial \eta$$
(1)

$$vgeos = \frac{g}{f} \frac{\partial \eta}{\partial x} (2)$$

- Where, x and y are the longitude and the latitude components respectively, n is the model SSH, g=9.81 m/s<sup>2</sup> is the gravity
- acceleration,  $f=2\Omega\sin(\lambda)$  is the Coriolis parameter,  $\lambda$  is the latitude in degrees and  $\Omega=2\pi/T$  is the Earth angular velocity,
- being T the period of rotation.

- 125 In order to evaluate the tidal residual from the full SSH signal, a Doodson filter was applied to the dataset, following the
- approach proposed in the Manual on Sea Level Measurement and Interpretation of the IOC (1985). The Doodson is a low-
- pass, symmetric filter based on the definition of 19 coefficients as follows:

128 
$$F(t) = (2, 1, 1, 2, 0, 1, 1, 0, 2, 0, 1, 1, 0, 1, 0, 0, 1, 0, 1); F(t) = F(-t)$$

The value of the de-tided sea level  $SSH_{res}$  at time  $t_0$  is calculated as:

$$SSH_{res}(t_0) = \frac{1}{30} \sum_{d=-19}^{d=19} F(d)SSH(t_0 + d); d \neq 0(3)$$

- Where SSH denotes the sea level elevation,  $t_0$  is the time expressed in hours and the coefficients d represent the increasing or
- decreasing hours with respect to the central value  $t_0$ .
- 133 **2.2.2** The normalized vorticity
- The normalized vorticity which is equivalent to the Rossbey number (RO) and is defined as (Poulain et al., 2023):

135 
$$\zeta^* = \frac{\zeta}{f}, \ \zeta = \frac{\partial v}{\partial x} - \frac{\partial u}{\partial y}(4)$$

- where  $\zeta$  is the relative vorticity,  $\zeta^*$  is a good indicator of features activity in the ocean. If  $\zeta^*\sim O(1)$ , the flow shows a-
- geostrophic features while for  $\zeta^*$ <<1 the flow shows quasi-geostrophic structures (Siegelman, 2020). For  $\zeta^*$ >0, indicates the
- presence of cyclonic structures, whereas for  $\zeta^*$  is negative the flow shows anticyclonic features.
- 139 **2.2.3** The normalized divergence
- 140 The normalized divergence, a fundamental metric to characterize the transport of passive and active tracers, is defined as
- 141 (Poulain et al., 2023):

142 
$$\delta^* = \frac{\delta}{f} , \ \delta = \frac{\partial u}{\partial x} + \frac{\partial v}{\partial y} (5)$$

- where  $\delta$  is the horizontal divergence of the velocity field. It allows to detect two different dynamical oceanic zones: for  $\delta^* >$
- 0(divergence) the flow fields tend to propagate outward through the surrounding surface of a closed control volume,
- diverging from its center, whereas for  $\delta^* < 0$  (convergence) the flow particles tend to converge to the center of the volume.
- 146 **2.2.4** The normalized Okubo-Weiss parameter
- 147 The normalized Okubo-Weiss parameter serves as a powerful indicator to distinguish between two different topological
- domains: elliptic or hyperbolic. It is defined as:

149 
$$Q^* = \frac{(S^2 - \zeta^2)}{(S^2 + \zeta^2)} (6)$$

- Where S is the strain or rate of deformation of the flow and it is composed by a shear term  $S_s$  and by a normal term  $S_n$ . It is
- 151 defined as follow:

$$S = \left[S_s^2 + S_n^2\right]^{\frac{1}{2}}(7)$$

Where  $S_s$  and  $S_n$  are defined as

$$S_s = \left(\frac{\partial v}{\partial x} + \frac{\partial u}{\partial y}\right)^2, S_n = \left(\frac{\partial u}{\partial x} - \frac{\partial v}{\partial y}\right)^2$$

Where  $Q^* = -1$  an elliptic domain can be defined, while where  $Q^* = 1$  a hyperbolic region can be identified (Okubo, 1970, Weiss, 1991, Elhmaidi et al., 1993; Bouzaiene et al., 2018, 2021). As shown by Bouzaiene et al. (2021), the flow dynamical properties in the eddy inner parts (elliptic regions) and surrounding coherent structures (hyperbolic structures) are very different. In this study S is normalized by f to identify the sheared and/or stretched regions:

$$S^* = \frac{S}{f}(8)$$

## 2.2.5 The Finite Time Lyapunov Exponent

The Finite Time Lyapunov Exponent (FTLE)  $\lambda_t$  is a parameter which describes the separation amongst particles in a specific time interval and it has been used in several ocean applications to identify the Lagrangian Coherent Structures (LCS) (Shadden et al., 2005; Farazmand and Haller, 2012). In previous investigations within the Mediterranean region, the emphasis was on the Finite Scale Lyapunov Exponent (FSLE) rather than the FTLE. The FSLE was calculated on the basis of the exponential growth of distances between Lagrangian particle pairs initially separated. This calculation served the dual purpose of identifying Lagrangian Coherent Structures (LCS), as demonstrated by d'Ovidio et al. (2004, 2009), and comparing LCS with Lagrangian surface drifter trajectories, as explored by Bouzaiene et al. (2020).

More recently, Morales-Márquez et al. (2023) investigated the use of FSLE to characterize LCS concerning mixing and transport properties in the upper layer of the entire Mediterranean Sea. Despite these advancements, the application of the parameter  $\lambda_t$  in coastal Mediterranean zones, particularly in the GG, remains an unanswered question. The implementation of

FTLE in coastal areas, namely from altimetry data, has been limited by the error of the data in very coastal areas. This study seeks to address this gap by computing  $\lambda_t$  specifically for LCS analysis in these areas.

FTLE is a local scalar that represents the separation rate of initially neighboring particles for a finite time [ $t_0$ ,  $t_0+T$ ]. At position  $x_0$  and time  $t_0$ ,  $\lambda_t$  is defined as follows (Haller, 2002, 2015; Liu et al., 2018):

$$\lambda_{t}(x_{0}, t_{0}, T) = 0.5 \left[ \frac{\log \lambda_{max} \left( \left[ \frac{\partial \Phi(x_{0}, t_{0} + T, t_{0})}{\partial x_{0}} \right]^{tr} \left[ \frac{\partial \Phi(x_{0}, t_{0} + T, t_{0})}{\partial x_{0}} \right] \right)}{T} \right]$$
(9)

defined as  $\Phi(x_0, t_0 + T, t_0)$  and it indicates the matrix transpose. In 2D turbulence theory, the eigenvalues of the Cauchy-Green tensor quantify the stretching of fluid particles along their relevant directions (Liu et al., 2018). FTLE can be implemented forward and/or backward in time and the implications for phytoplankton as one shows attracting and the other repelling structures. In this work, we compute the forward on time or positive-time (T>0) of  $\lambda_t$  field. This eigenvector is called "forward Finite-Time Lyapunov Vector". It has been shown that  $\lambda_t$  is predominantly reliable to capture coherent structures starting from an integration time of 6 days, with no upper limit (Du Toit, 2010; Rypina et al., 2011; Liu et al., 2018). In this study, daily FTLE fields are computed, and then averaged seasonally over a 30-year period to detect the mean features and over 7 days to compare it to phytoplankton blooms occurring in GG.

where  $\lambda_{max}$  is the largest eigenvalue of the Cauchy-Green stress tensor, while the flow field of fluid particle trajectories is

Here,  $\lambda t$  is calculated from the velocity fields derived from satellite altimetry data at temporal and spatial resolutions of 1 day and  $1/8^{\circ}$ , respectively. Our choice is to set the resolution of the mean initial trajectory conditions to 800 meters ×800 meters, corresponding to  $1/128^{\circ}$ , about 16 times larger than the velocity field resolution, which guarantees an LCS accurate enough for capturing oceanic features (Onu et al., 2015). In general, high values of  $\lambda t$  indicate the edges of coherent structures, fronts and filaments (hyperbolic regions), while low values correspond to the inner parts of the eddies (elliptic areas). Both are considered as transport barriers (Blazevski and Haller, 2014). Intense stirring induced by strong turbulence disperses the high input of nutrients when uplifted from deeper layers, whereas larger amounts of nutrients remain in more quiescent zones (decreased turbulence; Hernandez-Garcia et al., 2010).

3 Results

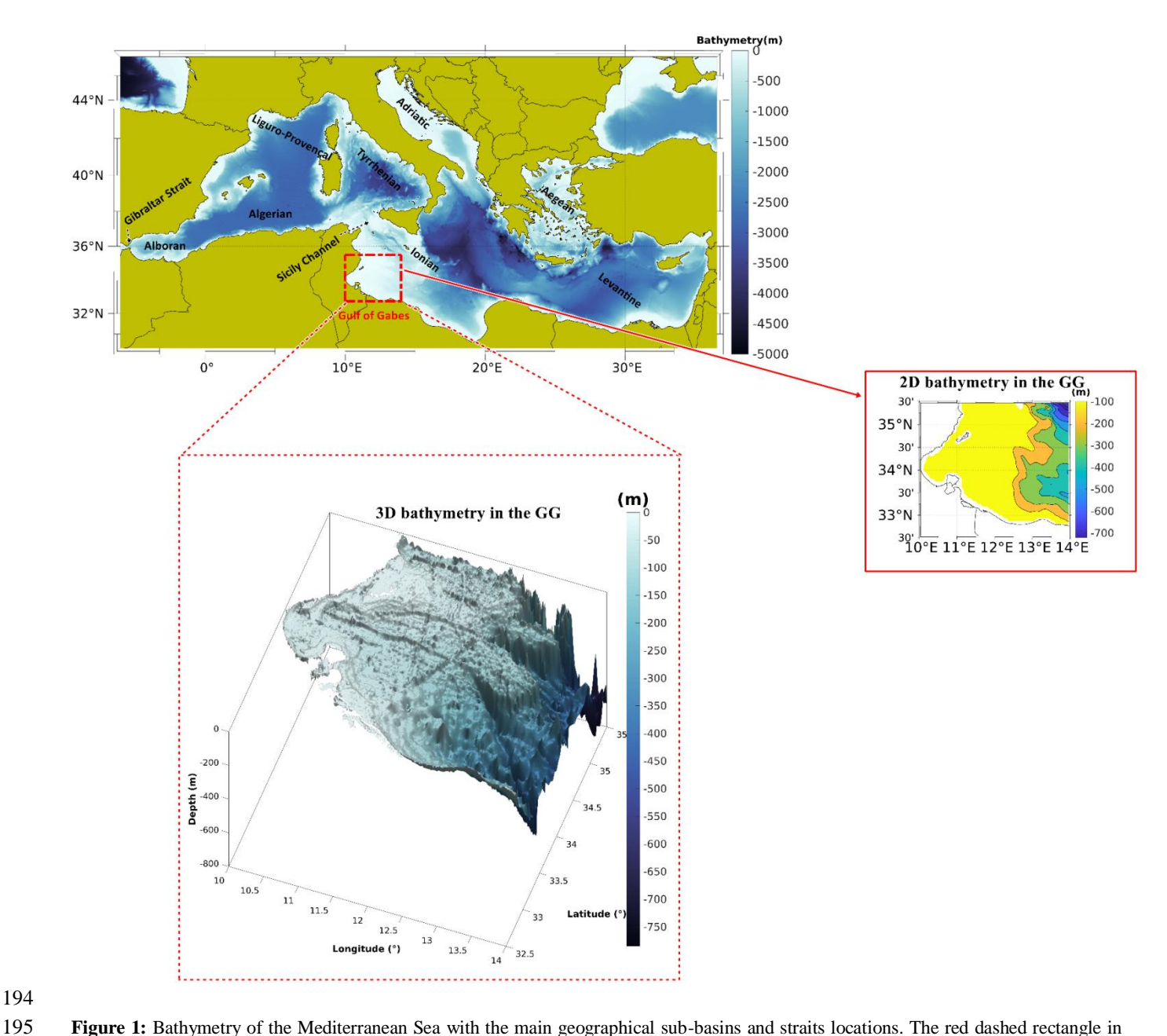


**Figure 1:** Bathymetry of the Mediterranean Sea with the main geographical sub-basins and straits locations. The red dashed rectangle in the upper panel shows the geographical limits of the larger Gulf of Gabès domain. Zooms of 2D and 3D bathymetry in the Gulf of Gabès are shown in the lower panels. The bathymetry was derived from the Global Earth Bathymetric Chart of the Oceans for the 2022 version with a spatial resolution of ~0.45 km (GEBCO\_2022, https://www.gebco.net).

Three subareas were identified in the GG (black boxes in Figure 2) in order to highlight differences and similarities in the dynamical features: Northern Gulf of Gabès (NGG, 11°E-12°E and 34.6°N-35.25°N), Central Gulf of Gabès (CGG, 10°E-11°E and 33.75°N-34.4°N) and Southern Gulf of Gabès (SGG, 11.1°E-12.2°E and 33°N-33.75N°). The Mediterranean features are strongly driven by the instability of intense coastal currents, which have frequently changed their location and lifespan over the past decades (Bouzaiene et al, 2020; Poulain et al, 2012). In order to investigate the kinematic properties of mesoscale features, we used 30 years of altimetry data in the present paper, focusing on the main circulation features in the GG. This 30 year dataset allows for the detection of mean patterns across three decades, providing a basis to discuss the well-known mean features during the observational data availability period. The 30 years of satellite altimetry data are used to overview the mean kinematic features in the GG domain and in the three specified subareas, as detailed in section 3.1.

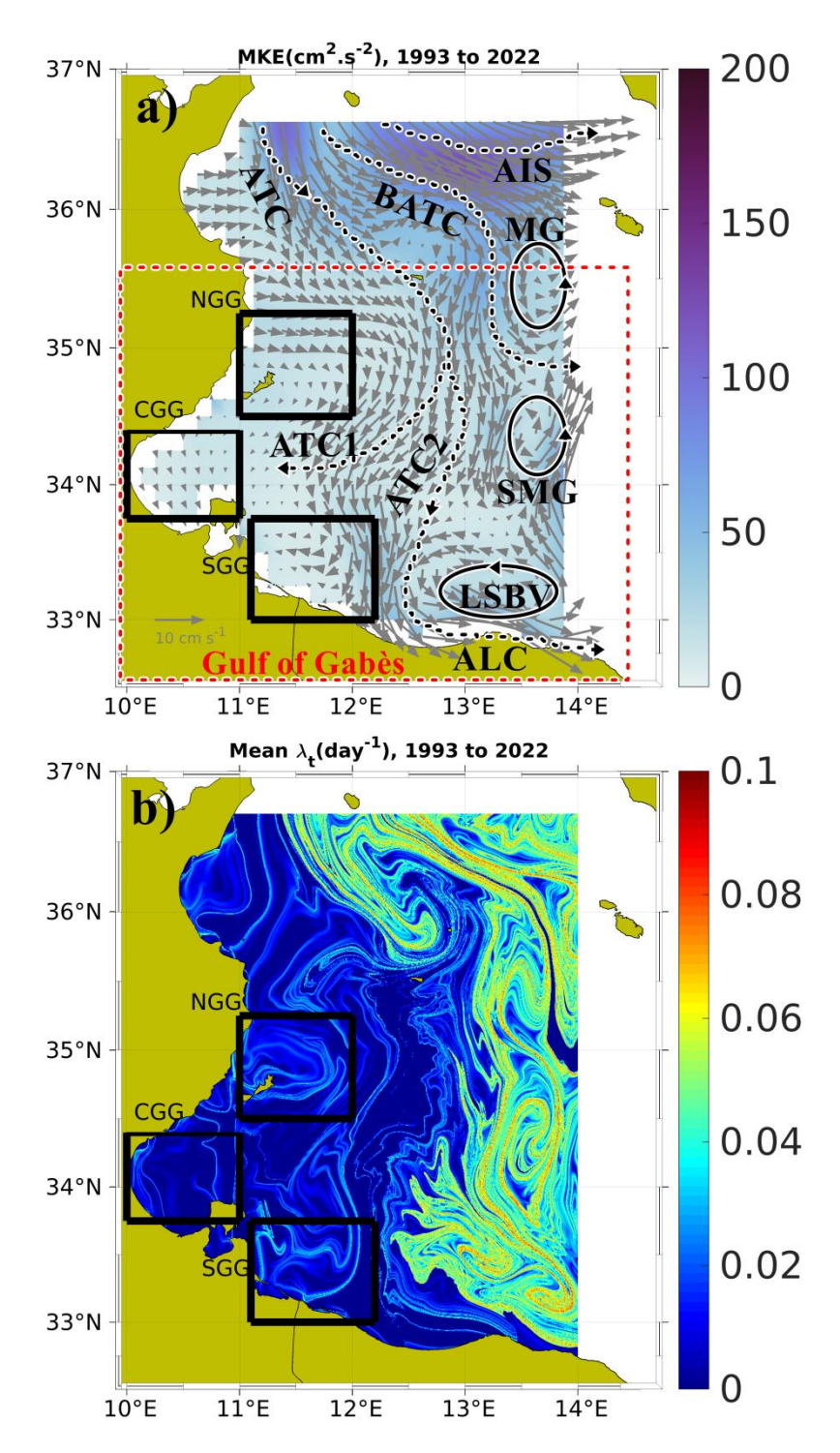


Figure 2: (a) Mean Kinetic Energy (MKE) with superimposed mean geostrophic currents estimated over the period 1993-2022; (b) Mean Finite Time Lyapunov Exponent ( $\lambda_t$ ) computed from geostrophic velocities from altimetry data

- 211 (SEALEVEL\_EUR\_PHY\_L4\_MY\_008\_068) in the same period. Three subareas are selected close to the coastal areas of the gulf as
- 212 follow: NGG: Northern Gulf of Gabès, CGG: Central Gulf of Gabès, SGG: Southern Gulf of Gabès. List of acronyms of the main
- 213 circulation features; MG: Medina Gyre, SMG: Southern Medina Gyre, LSBV, Libyan Shelf Break Vortex, ATC, Atlantic Tunisian
- 214 Current, ATC1, Fist Atlantic Tunisian Current, ATC2: Second Atlantic Tunisian Current, ALC: Atlantic Lybian Current, AIS: Atlantic
- 215 Ionian Stream, BATC: Bifurcation Atlantic Tunisian Current.
- The relatively low temporal and spatial resolutions of the data do not allow us to make considerations on the impact that
- 217 tides have on GG features in a smaller area. Hence, we focused on the GG Smaller Domain (CGG, 10.00°E-11.35°E and
- 218 33.40°N-34.75°N) where we derived geostrophic currents from the SSH model fields allowing us to test the tides impact in
- the GG, as explained in section 3.2. SSH spatial and temporal averages in the CGG have been removed from the native SSH
- 220 fields.

- The resulting mean seasonal geostrophic circulation in the CGG was compared to its counterpart computed from the de-tided
- 222 SSH fields, in order to assess the impact of tides on the geostrophic dynamics of the Gulf. The de-tiding on the native SSH
- fields was performed using a Doodson filter (see section 2.2.1 for details).

#### 3.1 Altimetry data analysis of the mean geostrophic circulation

- Figure 2a shows the geostrophic circulation (grey arrows) averaged over the period 1993-2022, superimposed to the Mean
- Kinetic Energy  $MKE = (0.5(ugeos^2 + vgeos^2))$  for the same period, where < ... > represents the average over the 30 years.
- 227 Several well-known structures are clearly visible, namely: (1) the edges of the cyclonic features referenced as the Medina
- 228 Gyre (MG), the Southern Medina Gyre (SMG) and the Libyan Shelf Break Vortex (LSBV); (2) the first Atlantic Tunisian
- 229 Current (ATC1) which is well developed along the Tunisian coasts; and (3) the second Atlantic Tunisian Current (ATC2),
- 230 flowing near the Libyan boundaries and forming the Atlantic Libyan Current (ALC), in agreement with the results of
- 231 Sorgente et al. (2011), Jebri et al. (2016) and Menna et al. (2019).
- The MKE shows the presence of energetic features flowing into the GG as well as surrounding eddies, BATC, ATC1 and
- ATC2 with MKE of ~50-100 cm<sup>2</sup>/s<sup>2</sup>, while the Atlantic Ionian Stream (AIS) inflows through the north-eastern Ionian Sea
- with a maximum MKE of approximately 100-150 cm<sup>2</sup>/s<sup>2</sup>. The mean FTLE averaged over the 30-year altimetry data period
- 235 ( $\lambda_t$ ; Equation 9) is shown in Fig. 2b.  $\lambda_t$  can be applied to investigate the link between the chaotic turbulence and the
- chlorophyll concentration, which are known to be related by inverse proportionality. The regions located far from the GG,
- 237 are characterized by a large  $\lambda_t$ , close to 0.1 day<sup>-1</sup>, indicating strong chaotic advection clearly evidenced by the presence of
- 238 intense eddies and persistent currents (MG, SMG, LSBV, AIS, see Figure 2a vs. 2b). These features appear as local barriers
- 239 to transport, inhibiting biological production. On the contrary, in the coastal zones of the GG,  $\lambda_t$  tends to zero. These zones
- 20) to transport, innothing officer production. On the Committee, in the Committee of the Co., in tends to 2010.

may favor the nutrient standing stocks due to the weak effect of the horizontal mixing and stirring. This could be one of the

- 241 causes of the observed high chlorophyll concentration close to the Tunisian boundaries as shown in previous studies (Bel
- 242 Hassen et al., 2010; Macias et al., 2018; Kotta et al., 2019), where nutrients would flee from high turbulent zones to settle in
- less chaotic areas.

The NGG is clearly evidenced by the presence of a large anticyclonic current with  $\lambda_t$ ~0 in its core, while  $\lambda_t$  is greater than zero in the eddy outer part. A similar pattern can also be observed in the SGG. On the contrary, the mean FTLE in the SGG suggests the presence of filaments and fronts (Fig. 2b). Normalized vorticity ( $\zeta^*$ ), normalized Okubo-Weiss ( $Q^*$ ), normalized divergence ( $\delta^*$ ), and normalized deformation ( $S^*$ ) over the 30 years (1993-2022) from the altimetry product are shown in Figure 3a,b,c and d, respectively, confirming the presence of the MG, SMG and LSBV eddies. Except for the MG, within the interior of these structures, the value of  $Q^*$  is negative (elliptic regions) due to high vorticity gradients, whereas in the surrounding coherent structures the value of  $Q^*$  is positive, with predominantly hyperbolic areas due to strong deformation gradients (Fig. 3b).

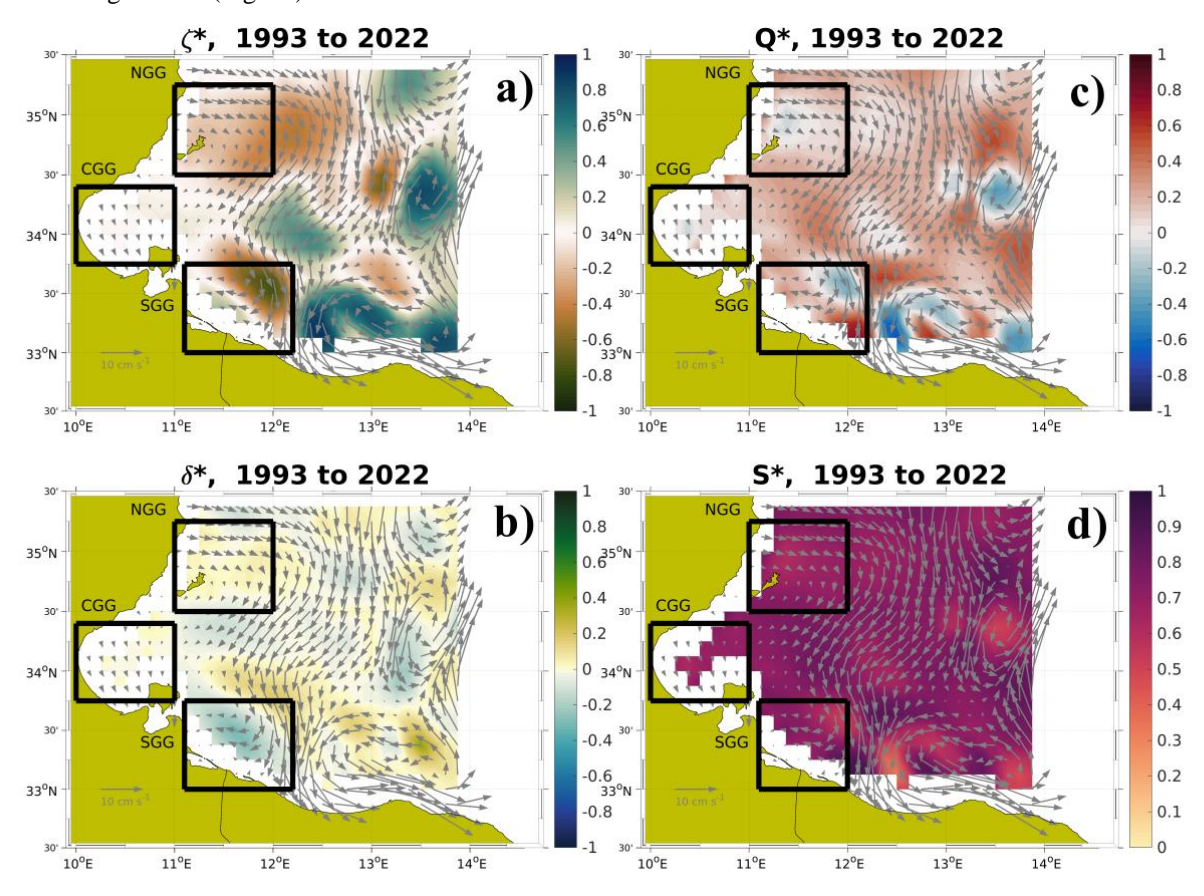
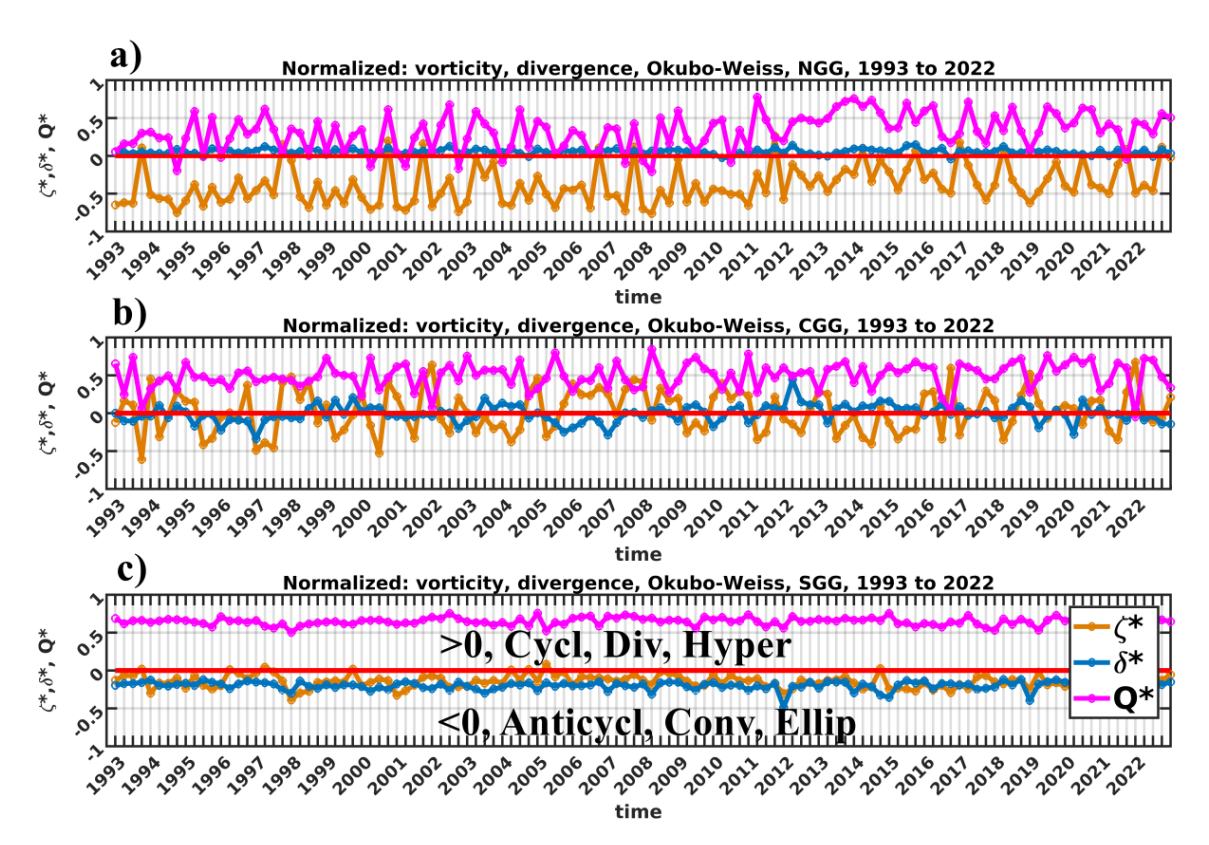


Figure 3: Mean circulation from altimetry data (SEALEVEL\_EUR\_PHY\_L4\_MY\_008\_068) estimated over the period 1993-2022 (a) Normalized vorticity ( $\zeta^*$ ), (b) normalized Okubo-Weiss parameter Q\*, (c) the normalized divergence ( $\delta^*$ ) and (d) normalized deformation (S\*) with superimposed mean geostrophic velocities. Three subareas are selected close to the coastal areas of the gulf as follow: NGG: Northern Gulf of Gabès, CGG: Central Gulf of Gabès, SGG: Southern Gulf of Gabès.

The vorticity mostly agrees with the divergence (Fig. 3a and c) for  $\zeta^*$  and  $\delta^*$  higher than zero, implying the presence of several cyclonic eddies where the flow tends to propagate outward through the surrounding eddy cores (divergence).

Upwelling of deep, nutrient-rich water masses occur in these areas, leading to enhanced biological production at the surface. In the opposite scenario (negative  $\zeta^*$  and  $\delta^*$ ) the surface flow is pointing towards the inner parts of the anticyclonic eddy (convergence), pushing water towards its center of mass, then sinking to the bottom layers. The flow is sheared or stretched (S\*~O(1)) in the eddy outer parts where the current is very unstable. These zones can be identified as hyperbolic regions due to strong deformation gradients, while for S\*~O (inside coherent vortices) the rotation is dominant (Figure 3 b and d). In order to compare the dynamics of regions relatively close to the GG with farther ones,  $\zeta^*$ ,  $\delta^*$  and  $Q^*$  are seasonally evaluated in the three sub areas displayed in Figure 4. They can all be classified as hyperbolic regions (Q\*>O, magenta lines in Figure 4) meaning that the flow can be stretched or sheared. Except for some seasons, the NGG and CGG surface waters tend to rotate into gyres (elliptic areas, Q\*<0). In the CGG, the vorticity is oscillating from ~-0.5 (anticyclonic) to ~0.5 (cyclonic), while  $\zeta^*$  shows mostly negative values in the two other areas considered (thus indicating the presence of anticyclonic vortices). In agreement with the vorticity values, the divergence is negative in the SGG (convergent flow, Fig 4c). In the NGG and CGG,  $\delta^*$  indicates positive values, mostly greater than zero in the NGG, thus denoting the presence of upwelling flows (Fig. 4a,b blue line). The difference in the divergence of the three subareas might be related to the different interaction of the main forces (i.e tides and winds) with the bottom topography.



**Figure 4:** Time series of normalized vorticity ( $\zeta^*$ ; yellow), normalized divergence ( $\delta^*$ ; blue) and normalized Okubo-Weiss parameter ( $Q^*$ , magenta) estimated from geostrophic velocities provided by altimetry data (SEALEVEL\_EUR\_PHY\_L4\_MY\_008\_068) in the Gulf of Gabès over the period 1993-2022. Panel (a): North GG; Panel (b): Central GG; Panel(c): South GG.

# 3.2 Model data analysis of the geostrophic circulation in 2022

The GG surface circulation is strongly controlled by tides (Zayen et al., 2020). The highest tidal ranges can be detected in the central part of the GG, whilst they are much less significant outside of the gulf (Abdennadher and Boukthir, 2006). Tidal movements, which induce vertical mixing, could be considered as a potential cause of high chlorophyll concentration in the CGG (Macias et al., 2018). As a preliminary step, before computing the quantities described in Section 2, we compared the geostrophic circulation derived from the daily altimetry product and model data with resolutions of 1/8° and 1/24°, respectively, in the larger GG domain in 2022, as shown in Figure 5. Both sources show similar circulation structures: SMG, LSBV, ATC1, ATC2, ALC, AIS and BATC (Figure 5). The model results are in good agreement with the observation where the impact of high resolution model data can be found in ATC1 intensity in CGG (Figure 5 b).

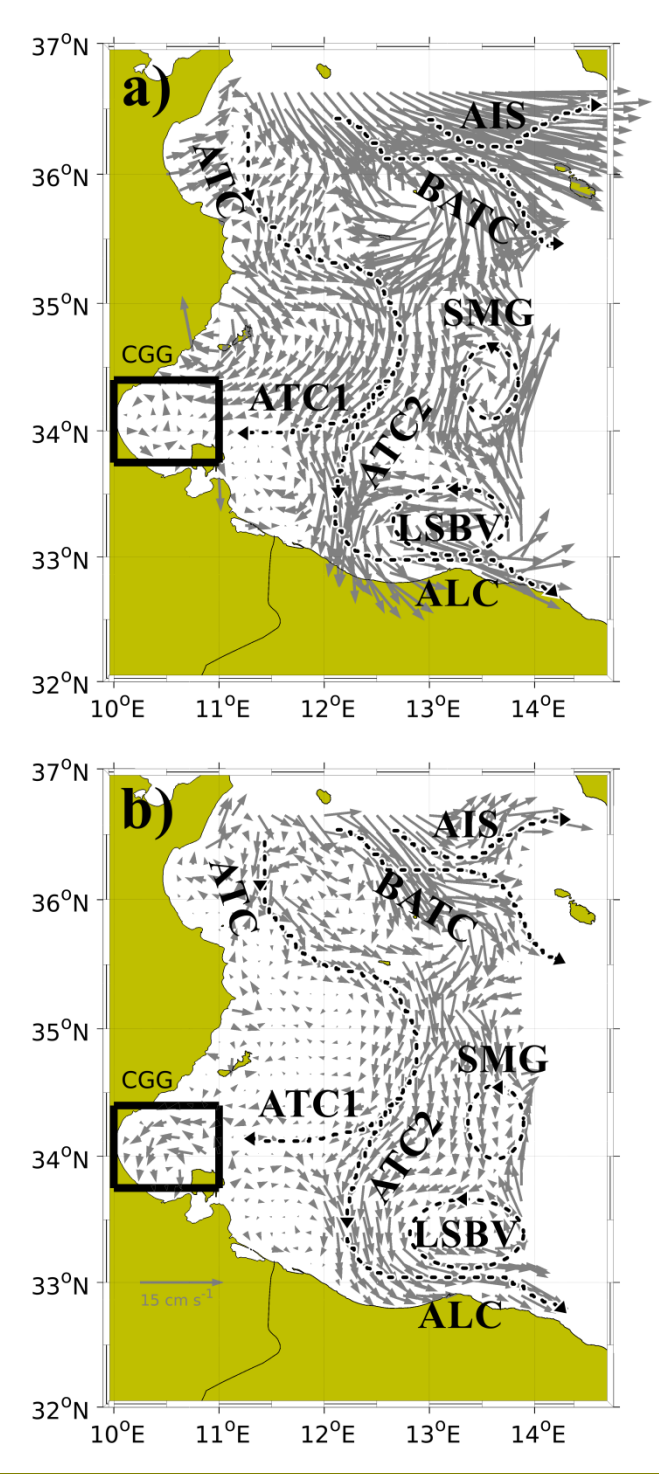


Figure 5: (a) Mean geostrophic currents derived from Altimetry product and (b) mean geostrophic currents derived from CMS model product estimated over the period 2022. List of acronyms of the main circulation features: SMG: Southern Medina Gyre, LSBV, Libyan

- Shelf Break Vortex, ATC, Atlantic Tunisian Current, ATC1, Fist Atlantic Tunisian Current, ATC2; Second Atlantic Tunisian Current.
- ALC: Atlantic Lybian Current, AIS: Atlantic Ionian Stream, BATC: Bifurcation Atlantic Tunisian Current.
- 293 The following sections will focus on the CGG dynamics, both because of its importance from the biological production point
- of view, as shown previously by Feki-Sahnoun et al. (2018), and because it represents a site of particular interest to
- investigate the influence of tidal forcing on dynamics.

### 3.2.1 Seasonal variability

296

297

298

299

300

301

302

303

304

305

306

307

308

309

310

311

312

313

314

315

316

317

The comparison of the mean seasonal geostrophic circulation in 2022 derived from full SSH and detided SSH is shown in Figures 6 and 7, where the arrows representing the geostrophic velocities are superimposed to the kinetic energy. During winter/fall the mean flow tends to inflow from the south to the north, while in spring and summer its circulation is mainly cyclonic bordering the coastline. Our results are in good agreement with previous studies in the Mediterranean Sea (Vigo et al., 2018a). The difference in flow direction in the CG can be related to the topography of the gulf (Figure 1) and/or to the horizontal pressure force influenced by anomalous cyclonic and anticyclonic atmospheric conditions which were present in 2022, as found in Marullo et al. (2023). These atmospheric conditions could also be potential causes of the different seasonal geostrophic patterns shown in Figure 6 and 7. The influence of tides can also be found in the difference of the seasonally averaged KE computed in the case of full SSH and detided SSH. In winter, in the case of geostrophic currents computed from full SSH, the KE can reach ~50 cm<sup>2</sup>/s<sup>2</sup>, while it decreases in the other seasons with the lowest values detected in summer/fall (KE <5 cm<sup>2</sup>/s<sup>2</sup>). The tides influence on geostrophic circulation can be also quantified by the differences in mean KE computed from full SSH and detided SSH fields. The largest MKE values (8.25 and 8.06 cm<sup>2</sup>/s<sup>2</sup> for tidal and detided fields, respectively) can be observed in winter, while the lowest values are observable in fall, with an average value of about 0.17/0.14 cm<sup>2</sup>/s<sup>2</sup>. In spring and summer, the MKE values of 2.06/1.3 and 0.43/0.23 cm<sup>2</sup>/s<sup>2</sup>, respectively. Moreover, in spring and summer the relative weight of the tidal component of the KE is much stronger (46% and 37% respectively) than in winter and fall (2% and 17%). Since tidal forcing itself does not have significant seasonal variability, it is clear that it does not affect the varying seasonal patterns shown in Figures 6a, c and 7a, c. The impact of tides on geostrophic circulation can be observed for the cyclonic vortex detectable in spring, summer and fall north-west of Dierba Island (~10.4E°-10.9E° and ~33.8N°-34.15N°, see the red lines in Figures 6 and 7) in the full SSH field, which disappears when deriving geostrophic circulation from detided SSH fields.

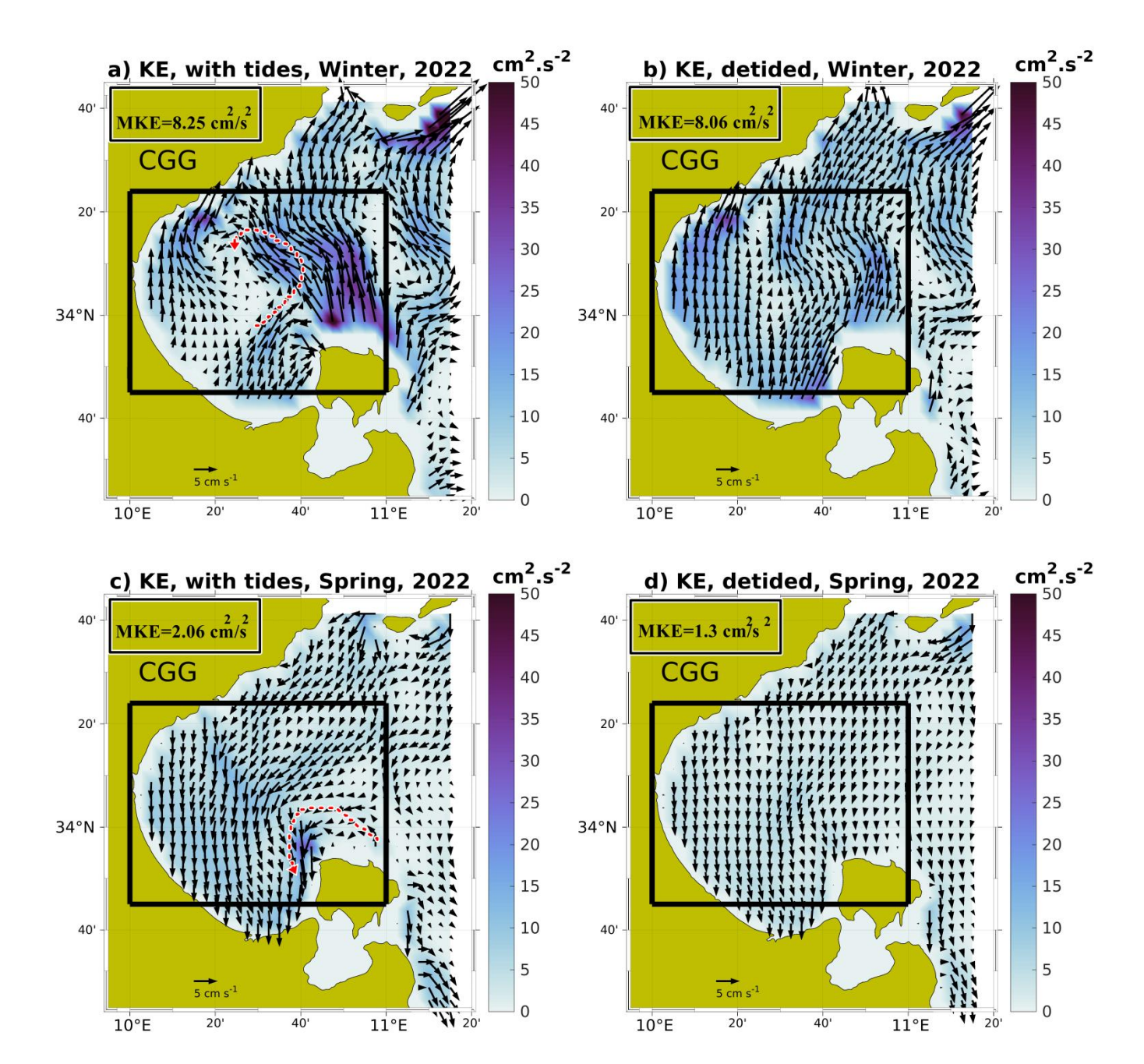


**Figure 6:** Seasonal mean geostrophic currents computed from MEDSEA\_ANALYSISFORECAST\_PHY\_006\_013 product SSH fields; both native with tidal forcing included (a, c) and detided (b, d) superimposed to seasonal Mean Kinetic Energy (MKE), in winter and spring, for the year 2022. The average MKE values are shown in the inserts. The black rectangles show the regions where tides impact on the circulation in the north-eastern part of the Djerba Island. The black rectangles show the CGG while the dashed red lines show the cyclonic currents.

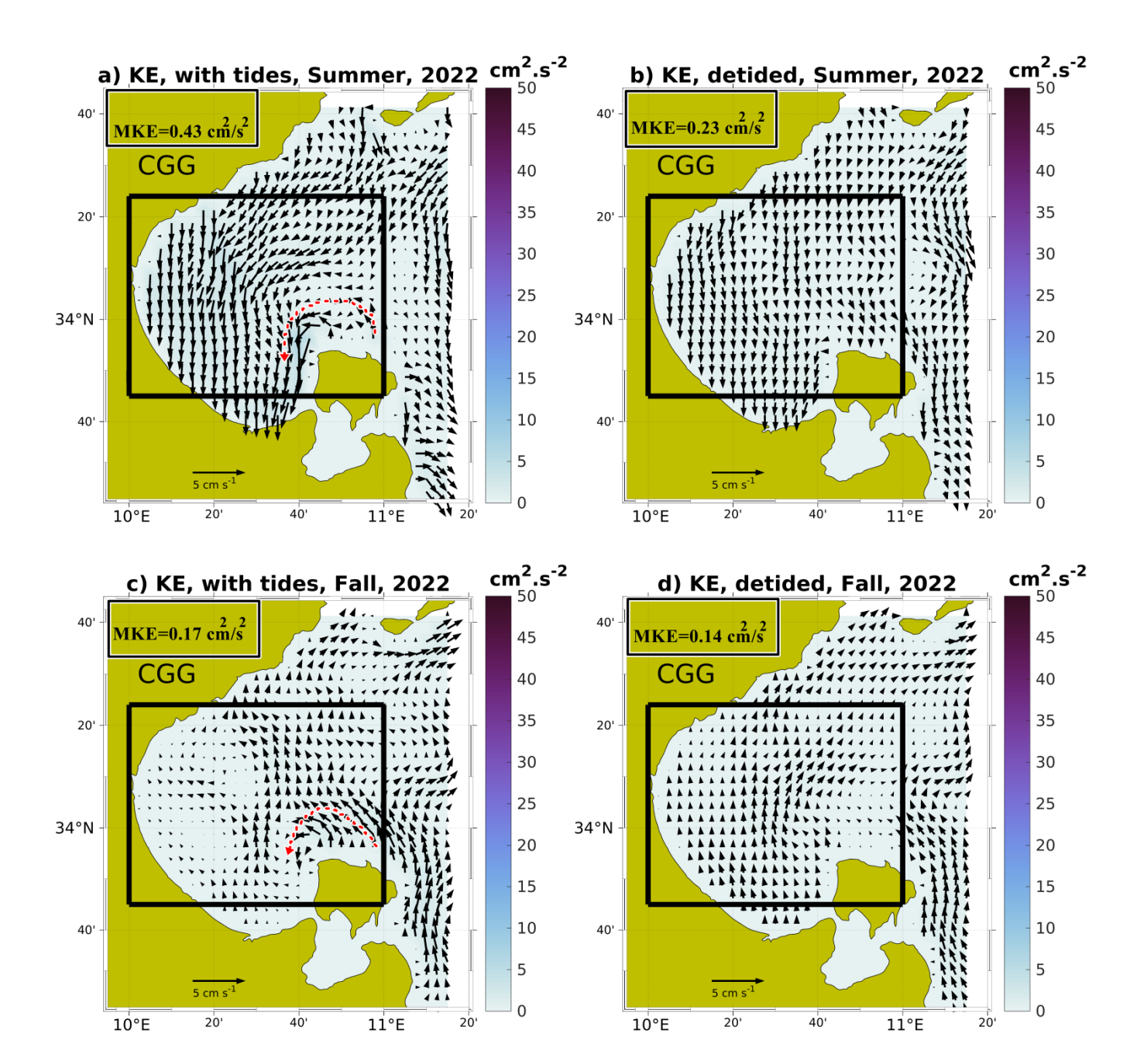


**Figure 7:** Seasonal mean geostrophic currents computed from MEDSEA\_ANALYSISFORECAST\_PHY\_006\_013 product SSH fields; both native with tidal forcing included (a, c) and detided (b, d) superimposed to seasonal Mean Kinetic Energy (MKE), in summer and fall for the year 2022. The average MKE values are shown in the inserts. The black rectangles show the regions where tides impact on the circulation in the north-eastern part of the Djerba Island. The black rectangles show the CGG while the dashed red lines show the cyclonic currents.

We quantified the impact of tides on the dynamics of the CGG by computing the normalized Okubo-Weiss parameter Q\* (eq. 6) from the geostrophic currents derived from the model SSH fields in 2022. The results are displayed in Figures 8 a, c and 9a, c for the full signal and Figures 8 b, d and 9b,d for the tidal residual. Analyzing the geostrophic circulation derived from full SSH fields in the CGG, the study area can be classified as a hyperbolic region throughout all the seasons, with a value of Q\* clearly close to 1 for most of the time (>90%), due to strong deformation gradients. On the contrary, the diminished effect of rotation on CGG topology can be clearly observed for a small portion of the study area (<8%), where values of Q\* are close to -1.

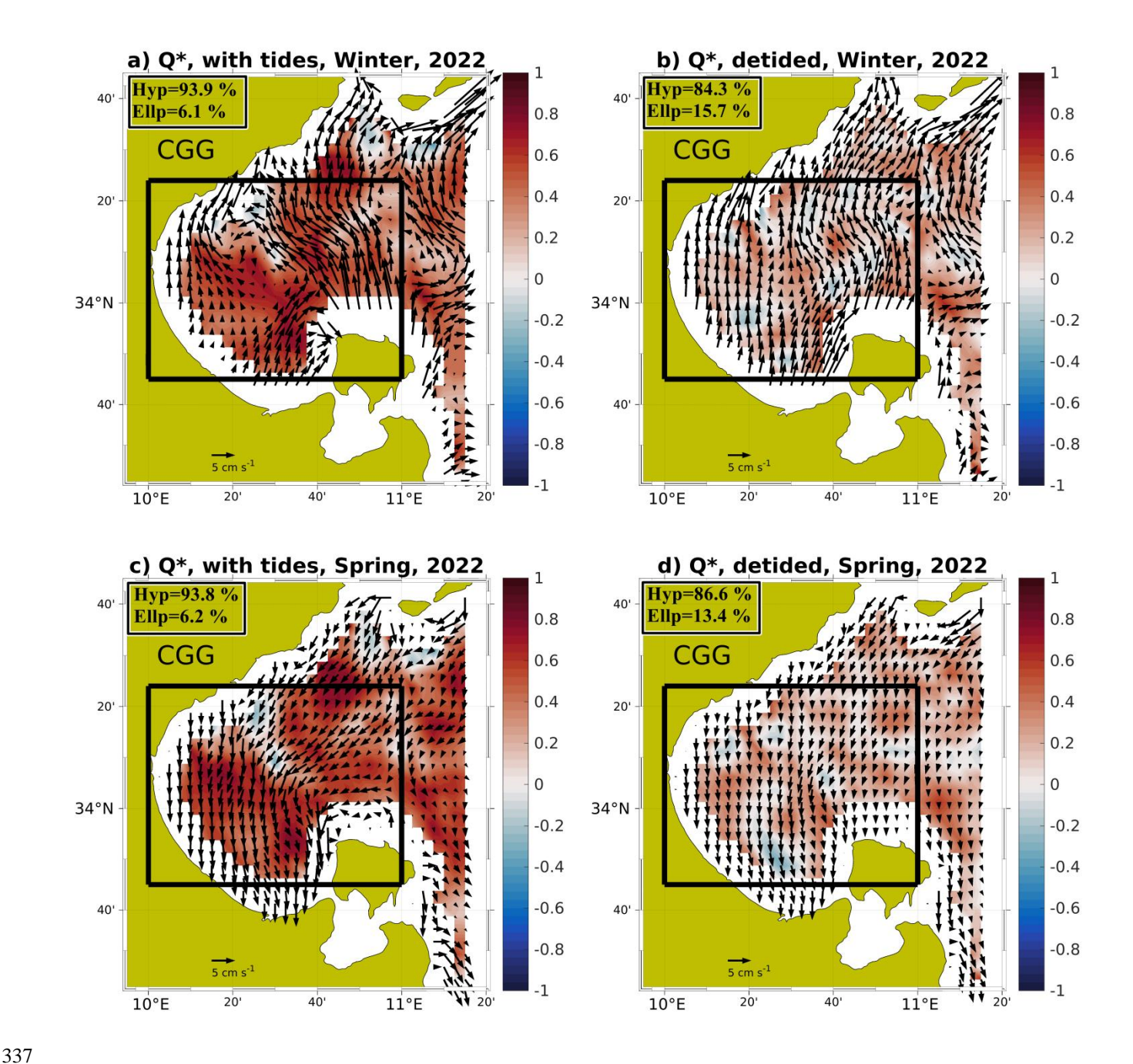


**Figure 8:** Seasonal mean normalized Okubo-Weiss parameter Q\* with superimposed mean geostrophic currents computed from MEDSEA\_ANALYSISFORECAST\_PHY\_006\_013 product SSH fields, both native with tidal forcing included (a, c) and detided (b, d), in winter and spring for the year 2022. The inserts show the percentage of the domain where Q\*<0 (elliptic grid cells) and Q\*>0 (hyperbolic grid cells). The black rectangles show the CGG.

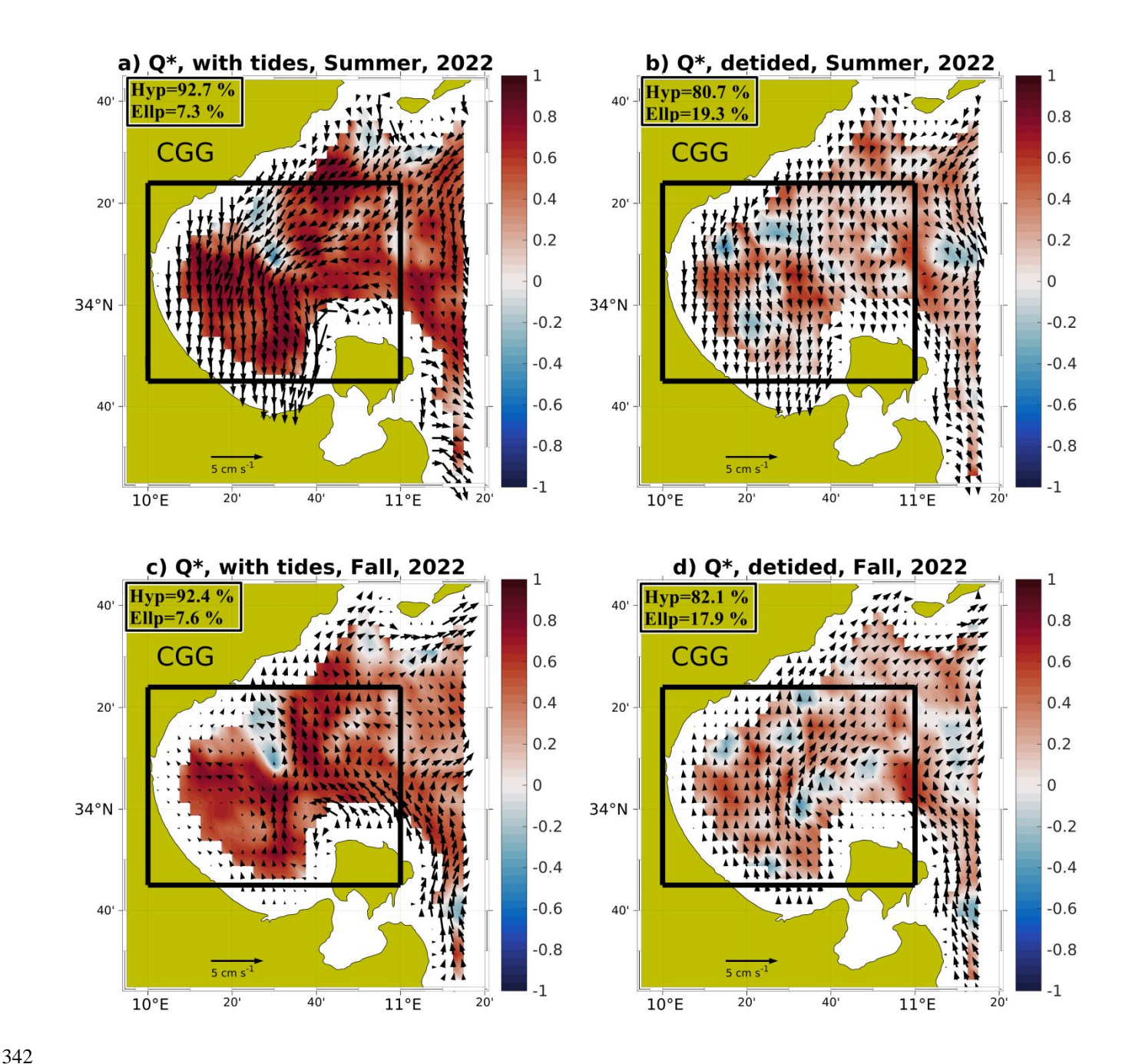


**Figure 9:** Seasonal mean normalized Okubo-Weiss parameter Q\* with superimposed mean geostrophic currents computed from MEDSEA\_ANALYSISFORECAST\_PHY\_006\_013 product SSH fields, both native with tidal forcing included (a, c) and detided (b, d), in summer and fall for the year 2022. The inserts show the percentage of the domain where Q\*<0 (elliptic grid cells) and Q\*>0 (hyperbolic grid cells). The black rectangles show the CGG.

The highest elliptic grid cell percentages were detected in summer (7.3%) and fall (7.6%) where the flow becomes more meandering than in winter and spring. By removing the tidal signal from SSH fields a decrease of ~10% of the hyperbolic areas (Figures 8 b, d and 9b, d) can be observed. In contrast, an increase of ~10% of elliptic regions can be noticed, with the flow becoming meandering. In general, the CGG is dominated by hyperbolic regions, and the presence of tides clearly enhances this tendency by approximately 10%. A possible explanation of the dominating hyperbolic structures even in the case of absence of tides might be related to the impact of wind on geostrophic circulation. Similar results were found in the Black Sea (Bouzaiene et al., 2021) where the hyperbolic regions are strongly dominant in winter due to larger wind stress, while in summer the elliptic areas are more pronounced because of the meandering currents.

# 3.2.2 Impact of tides on strain and turbulence

In order to confirm that tidal forcing is amplifying the deformation rate S\* that could increase the recorded hyperbolic grid cells found in Figures 8 and 9, we computed the normalized deformation rate both from full SSH (case 1) and detided SSH (case 2) fields and the corresponding time series are shown in Figure 10. In the presence of tides (blue dots) the S\* is larger than in the absence of tides (red dots) throughout the entire considered period. The difference between S\* in the two cases has an average of approximately 0.1 (yellow dots) meaning that tides produce stretching/deformation rates in the CGG and potentially enhance the presence of hyperbolic regions.

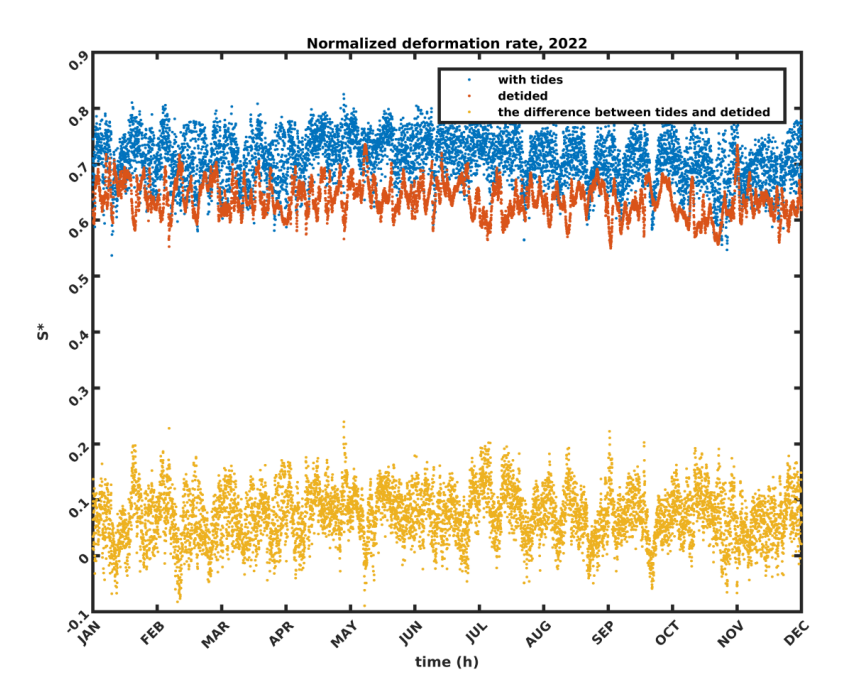


**Figure 10:** Time series of the deformation rate (S\*) computed from MEDSEA\_ANALYSISFORECAST\_PHY\_006\_013 product in 2022: full SSH fields (blue curve), detided SSH fields (red curve) and their difference (yellow curve).

To investigate tides influence on CGG, turbulence the Probability Density Function (PDF) of the normalized vorticity ( $\zeta^*$ ) has been computed on a seasonal basis in the two different cases mentioned above and the results are shown in Figure 11. In

the case of a 2D theoretical isotropic and homogeneous turbulent flow, PDF shows a Gaussian shape without intermittency (absence of tails).

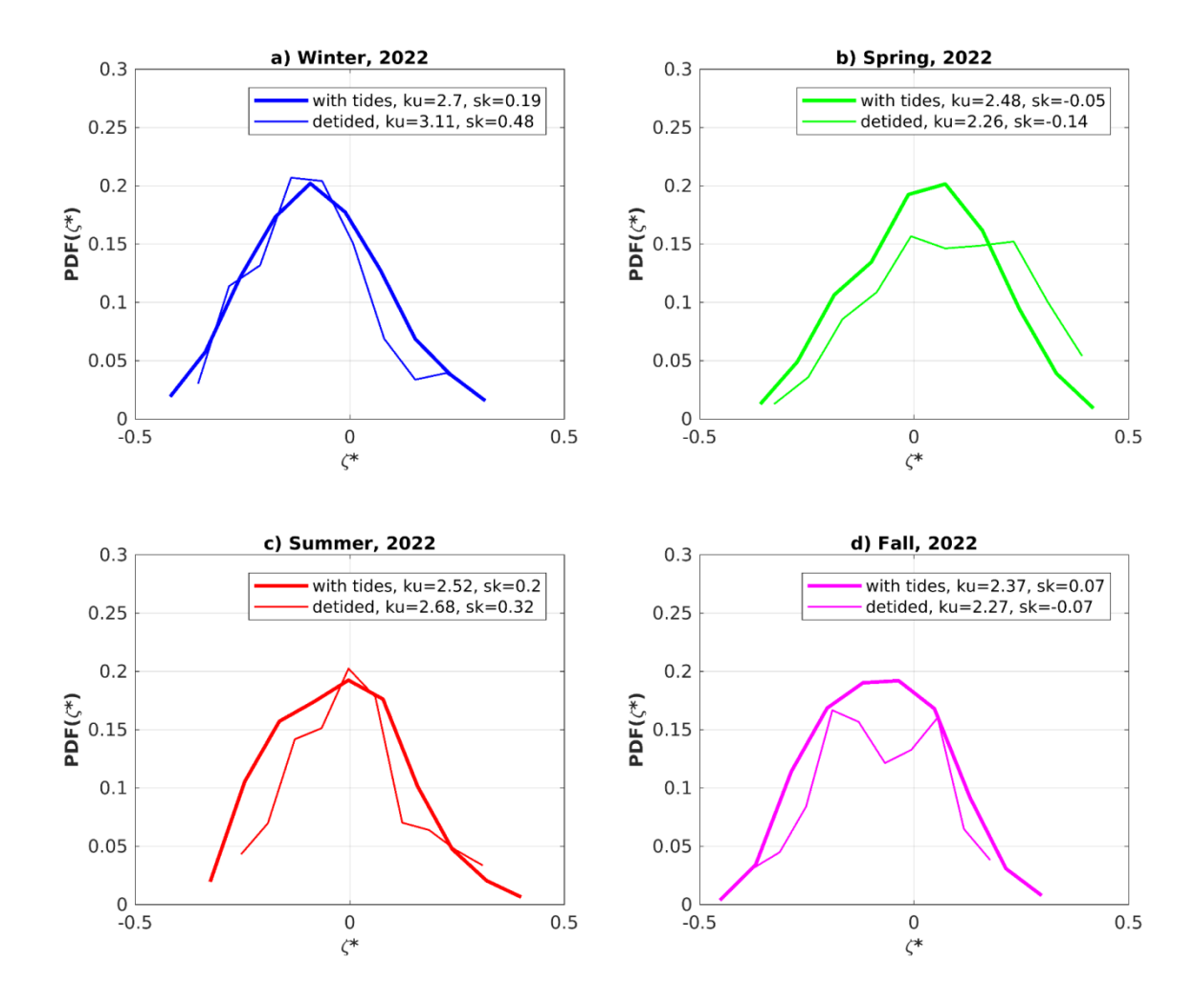


**Figure 11:** Seasonal Probability Density Function (PDF) of normalized vorticity ( $\zeta^*$ ) computed from MEDSEA\_ANALYSISFORECAST\_PHY\_006\_013 product in 2022: full SSH fields (bold curves) and detided SSH fields (thin curves) in (a) winter, (b) spring, (c) summer and (d) fall.

In our study the PDFs exhibit nearly Gaussian shapes. These appear to be regular shapes for all the seasons in case of flow affected by tides, with observable intermittency (long tails, ~-0.4 to 0.4) associated to the presence of coherent structures. The first case (SSH fields including tides) is well known as 2D quasi-geostrophic turbulence. Different Kurtosis and Skewness values depending on the season have been found. Low skewness values were detected in spring (sk=-0.05) and in fall (sk=0.07). Larger values were found in winter (sk=0.19) and summer (sk=0.2), with corresponding Kurtosis values of

2.48, 2.37, 2.7 and 2.52, respectively. The difference in Skewness and Kurtosis is essentially due to: (1) non-homogenous and anisotropic turbulent flow, (2) the influence of coherent vortices, (3) the presence of stretching/deformation. The anisotropic flow for asymmetric PDFs may be due to the asymmetry in flood and ebb tidal currents (Song, et al., 2007). For the 2nd case (i.e., the non-tidal forcing CGG dynamic) the shapes of all the normalized vorticity PDFs are irregular.

The central part of the GG is dominated by the presence of cyclonic eddies where the divergence is mostly positive as shown in Figure 4. The dynamics in the central GG region, as shown through the analysis of the altimetry data, is very different with respect to its northern and southern subareas, where prominent filaments and upwelling currents enhance phytoplankton blooms. Furthermore, the CGG, as shown through model data analysis, is rich in tidal activity, leading to the generation of cyclonic currents and relevant hyperbolic regions characterized by shearing and stirring oceanic flows. The tidal perturbation may impact the mixed layer, promoting upwelling processes that supply nutrients to the euphotic zone. The correlation between chlorophyll-a and FTLE over the study area could provide insights into the time lag between physical forcing and biological response. Phytoplankton bloom dispersion, compared to FTLE, can serve as an example of how metrics like FTLE can be used to illustrate the physical control of biogeochemical processes.

One of the possible applications of the results of our work is the study of the dispersion of nutrients connected to phytoplankton bloom events occurred in the GG and captured by NASA satellite images in March 2013 and 2017 as shown in Figure 12. The concept behind this application is to enhance the knowledge on how physics drives biogeochemistry: by comparing the phytoplankton blooms to the  $\lambda_t$  integrated over 7 days for high resolution of initial particle grid positions of  $1/128^{\circ}$ , this method may effectively enhance our comprehension of the link between physical processes and biogeochemistry. The qualitative correlation between algal bloom and  $\lambda_t$  shows how this latter can be used as a proxy for the distribution of the biomass and nutrients within the gulf. The positive divergence detected in the central Gulf of Gabès (Fig. 4b) explains the tendency to upwelling in this area (Poulain, 1993). The surface chlorophyll concentration from CMS multisatellite observations at 1 km resolution is displayed in the inserts of Figure 12 along with the phytoplankton blooms captured from NASA (March 12, 2013, March 23, 2017). A link between physics (FTLE) and biogeochemistry (Chl-a bloom) is noticeable, with the chl-a being dispersed on the edges of the GG coherent structures.

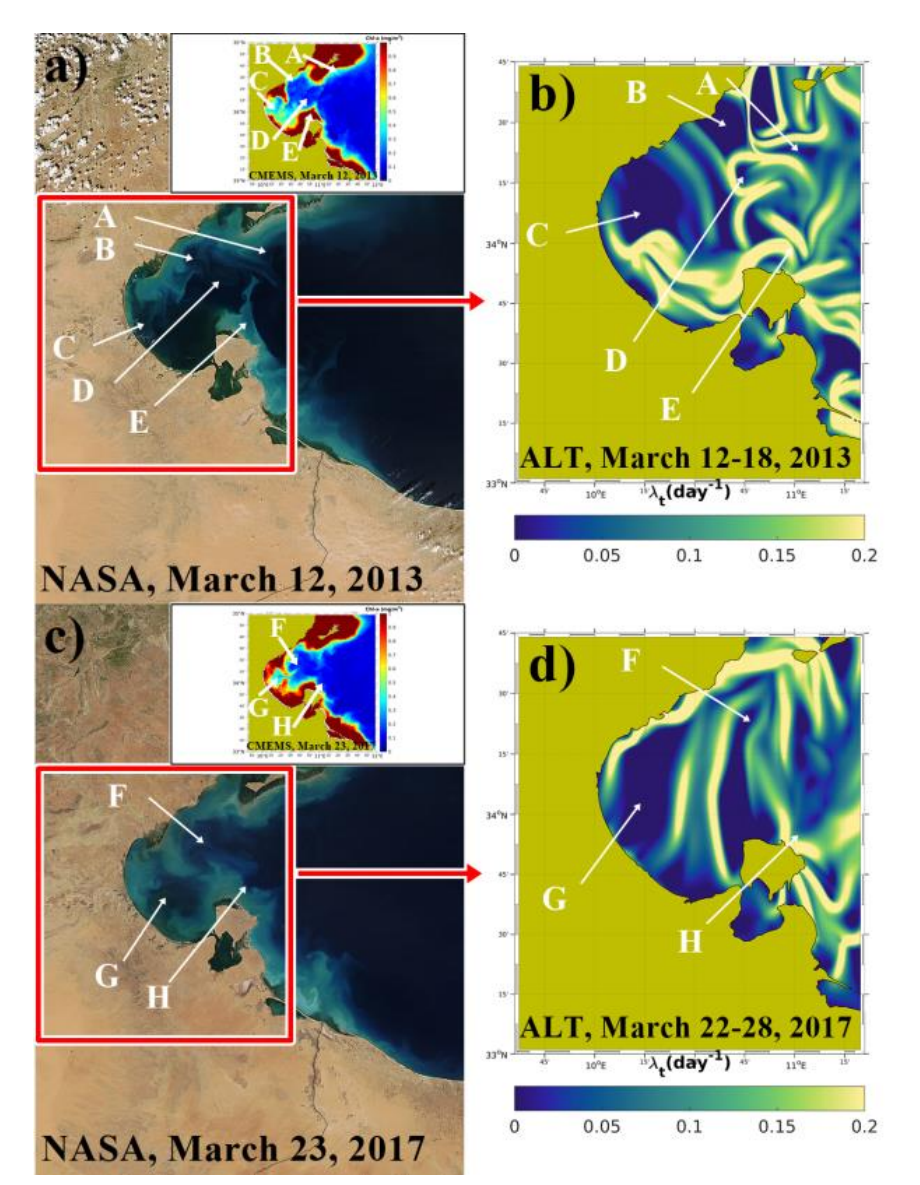
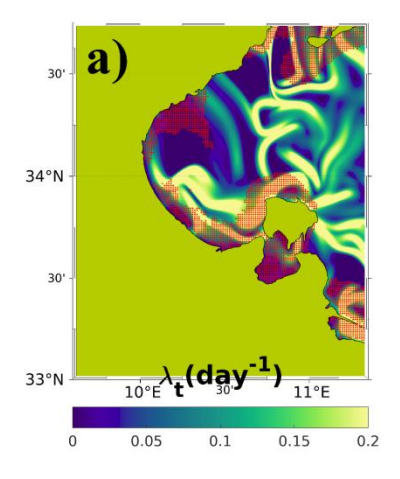


Figure 12: (a) Phytoplankton bloom off the coast of Tunisia-NASA MODIS Image of the Day, March 12, 2013 (https://modis.gsfc.nasa.gov/). (b) Spatial distribution of λ<sub>t</sub> computed from altimetry data (SEALEVEL\_EUR\_PHY\_L4\_MY\_008\_068) for 12-18 March 2013. (c) Phytoplankton blooms in the GG from NASA on March 23, 2017 and (d) spatial distribution of FTLE for 22-28 march 2017. Labels as A, B, C, D, E, F, G, H denote the features detected by NASA. In the insets we show chlorophyll a concentration from the European Union-Copernicus Marine Service (2022) for the same period as phytoplankton blooms were captured by NASA. This area is therefore the natural location for a high concentration of nutrients, favored also by the presence of cyclones (Salgado-Hernanz et al, 2019). GG features appear as transport barriers for phytoplankton dispersion. The phytoplankton blooms are driven by fronts, filaments, and mesoscale structures labeled as A, B, C, D, E, F, G and H in Fig. 9. A similar scenario has been observed in the northeastern Atlantic Ocean, where phytoplankton spring blooms are modulated by the

mesoscale dynamics. It has been found that mesoscale stirring due to the geostrophic circulation generates mesoscale chlorophyll structures (Lehahn, et al., 2007) in that region. The study shows that  $\lambda_t$  is a good indicator of phytoplankton blooms.

Starting from the hypothesis adopted in Suthers et al. (2023), i. e. that frontal eddies interacting with boundary currents may provide a suitable offshore nursery habitat, we filtered the OCEANCOLOUR\_MED\_BGC\_L4\_MY\_009\_144 dataset in order to define the areas of the domain with Chl-a concentration larger than 0.6 mg/m³. Then we superimposed these areas to the FTLE fields for the same aforementioned phytoplankton bloom events in 2013 and 2017 (see Figure 13). Numerous Chl-a were dispersed into GG frontal boundary eddies in both cases. Therefore, the GG coastal fronts appear to be the most significant driver for phytoplankton blooms dispersion. FTLE can be thus a useful tool to follow/predict phytoplankton blooms and nutrients advection.



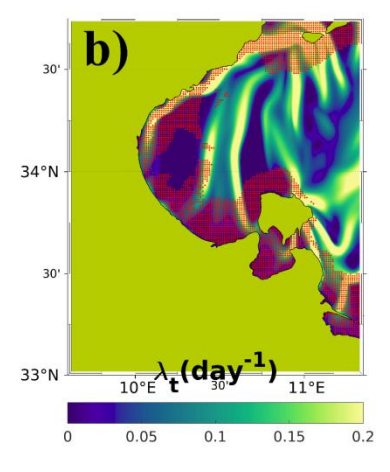


Figure 13: (a) Spatial distribution of  $\lambda_t$  computed from altimetry data (SEALEVEL\_EUR\_PHY\_L4\_MY\_008\_068) for 12-18 March 2013 superimposed with chlorophyll a concentration (Chl-a >0.6 mg/m³, red dotted areas), from the European Union-Copernicus Marine Service (2022) for 12 March 2013. (b) Spatial distribution of  $\lambda_t$  computed from altimetry data

427 (SEALEVEL\_EUR\_PHY\_L4\_MY\_008\_068) for 22-28 March 2017 superimposed with chlorophyll a concentration (Chl-a >0.6 mg/m³,

red dotted areas) from the European Union-Copernicus Marine Service (2022) for 23 March 2017.

### 4 Summary and conclusions

In this work the main hydrodynamic features of the Gulf of Gabès were investigated by means of geostrophic velocities derived from 30 years of satellite altimetry data and 1 year (2022) of hourly SSH fields produced by a high resolution oceanographic numerical system. Altimetry analysis of the GG is presented in terms of normalized vorticity ( $\zeta^*$ ), normalized divergence ( $\delta^*$ ), normalized Okubo-Weiss (Q\*), normalized deformation (S\*) and FTLE ( $\lambda_t$ ), to have an overview of the main circulation features (and their seasonal variability) of the GG. The mean spatial distribution of  $\lambda_t$  (1993-2022) confirms the presence of well-known features in the study area, such as ATC, MG, SMG and LSBV. The signature of these features can be found in the intensity of  $\lambda_t$  (Fig. 2b). The FTLE is a powerful diagnostic tool for ocean turbulence and horizontal mixing/stirring which vary inversely with phytoplankton concentration (Hernandez-Garcia et al., 2010). This may explain the poverty in nutrients in regions relatively far from the GG where we detected high values of  $\lambda_t$ , and it is in agreement with the known high biological production in areas close to the coast, where we found low values of  $\lambda_t$ . The different statistics show the presence of three different dynamical areas close to the GG coastal zones; North Gulf of Gabès (NGG), Central Gulf of Gabès (CGG) and Southern Gulf of Gabes Gabès (SGG).

The CGG subarea can be considered a zone rich in nutrients (since  $\delta^*$  showed some positive values) where the flow tends to spread particles. The application of  $\lambda_t$  method on altimetry data is shown to be a key tool to understand how GG dynamics drive passive organic tracers or pollutants. This scenario is observed for some seasons, with the divergence positive curve indicating the divergence of the CGG flow and explaining the phytoplankton blooms previously observed by Feki-Sahnoun et al. (2018). Furthermore, in the coastal zones located in the NGG the flow tends to be neutral ( $\delta^*\sim0$ ), except for some seasons when  $\delta^*$  is larger than zero, maybe due to the presence of upwelling events close to Djerba Island. In contrast, in the SGG, the flow is convergent, since it is characterized by a negative value of  $\delta^*$ . In this latter case the vorticity is concomitantly negative due to the signature of an anticyclonic vortex.

Geostrophic coastal currents and eddies are associated with the presence of hyperbolic regions (Q\*>0) in any season, with a crucial role played by stretching/deformation gradients (Figs 3 and 4).

The satellite data observations are limited in the CGG, especially close to the boundaries not allowing to study tidal signal impact on geostrophic circulation. We used a high resolution model data to focus on tidal signal impact on geostrophic pattern and topolology (i.e., the distribution of elliptic and hyperbolic regions). To the best of our knowledge, this paper for the first time discusses how tides affect the CGG flow topology. The flow topology has been related to anomalous absolute dispersion regimes in the Mediterranean Sea (Bouzaiene, et al., 2018) and the Black Sea (Bouzaiene, et al., 2021). Tides amplify hyperbolic regions in the CGG, with more than 90% of hyperbolic grid cells (Q\*>0) captured in any season, while elliptic regions almost disappear due to the outgrowth of hyperbolic ones. We also observed a significant change in geostrophic circulation pattern through the different seasons, as discussed in Figs. 6 and 7. These different patterns could be related to gulf topography, current instability and horizontal pressure gradients influenced by other atmospheric components.

- Waves in a coupled hydrodynamic-wave model can be an important factor affecting the geostrophic field as shown by other studies (Morales-Marquez et al 2023, Ruhs et al, 2025). A lower number of data observations were observed within the GG coastal areas as mentioned in model QUID where the RMSD of SLA increases significantly. This discrepancy can be reduced in the model itself since it was combined with data assimilation. In regions or time scales where geostrophic components become significant, given that the model includes tidal forcing and wave coupling, we might not be in geostrophic balance anymore. In the Mediterranean Sea, given that the high resolution model includes waves and tides, it
- offers an accurate geostrophic circulation (Escudier et al, 2021).
- Lower MKE values are recorded in summer and autumn, while higher values are detected in winter/spring. Since marine species disperse in regions characterized by lower turbulence and less energy intensity, our findings are in good agreement with the results found in Solgado Hernanz et al. (2019), where enhanced chlorophyll distribution in the CGG starts in June, peaks in September and terminates in February.
- Another finding of this study is the way tides contribute to stretching/deformation (S\*) to define the signature of the hyperbolic regions. The time series of S\* derived from geostrophic currents computed from the full SSH fields shows larger values with respect to the one computed from detided SSH fields. This confirms that tides are dynamically responsible for the amplification of deformation gradients. PDFs emphasize the non-homogeneity and anisotropy of the CGG turbulent flow due to the presence of eddies and intense strain factor.
- 477 To conclude, altimetry data available for the period of 1993–2022 was analyzed in the larger Gulf domain by comparing the 478 dynamics in three subareas and defining their common characteristics. The central part of the gulf is dominated by an 479 upwelling flow (thus characterized by divergence) where there is an important biological production rate. The other areas 480 located in its northern and southern parts are dominated by anticyclonic structures. The three subareas can be classified as 481 hyperbolic regions (Q\*<0). The high spatiotemporal resolution of model outputs allowed to analyze also the CGG over the 482 year 2022. In good accordance with the altimetry analysis, the CGG can be classified as hyperbolic area with a signal greater 483 than 90%, whereas the signature of elliptic zones is lower than 10%. Atmospheric conditions, topography and tides forcing 484 are very important for the occurrence of hyperbolic regions driven by strain. As well as amplifying hyperbolic regions, tides 485 also affect the isotropy and homogeneity of the theoretical turbulent flow. PDF is applied to quantify the impact of tides on 486 2D turbulence theory and the PDF asymmetric distributions reveal the non-homogeneity and anisotropy of the surface flow 487 due to persistent stretched currents and eddies.

- Data availability. This study has been conducted using E.U. Copernicus Marine Service Information. The products used are MEDSEA\_ANALYSISFORECAST\_PHY\_006\_013 (Clementi et
- 491 al.2023,https://doi.org/10.25423/CMCC/MEDSEA\_ANALYSISFORECAST\_PHY\_006\_013\_EAS8),
- 492 SEALEVEL\_EUR\_PHY\_L4\_MY\_008\_068 (European Union-Copernicus Marine Service 2021,
- 493 https://doi.org/10.48670/MOI-00141) and OCEANCOLOUR\_MED\_BGC\_L4\_MY\_009\_144
- 494 ((https://doi.org/10.48670/moi-00300, Mediterranean Sea Ocean Satellite Observations, the Italian National Research

- 495 Council (CNR Rome, Italy)) which are made available through the Copernicus Marine Data Store
- 496 (https://data.marine.copernicus.eu/products).

- 498 Author contributions. Formal analysis, conceptualization, methodology, investigation, writing original draft preparation:
- 499 MB. Data curation: AG. Funding acquisition: SS. Writing review and editing: MB, AG, DD, AFD, SS and CF. All the
- authors have read and agreed to the published version of the paper.

501

- 502 Funding. This research was funded by the Italian Ministry of University and Research as part of the NextData project.
- 503 Competing interests. The authors have no competing interests.

504

- 505 Acknowledgments. We thank G. Haller and K. Onu for providing the code for FTLE computation in this study. Special thanks
- 506 to my father, I am grateful for the many years you were my guiding star, my best gratitude to you, I will never forget your
- kindness and support even after your death.

508 References

- Abdennadher, J., and Boukthir, M. (2006). Numerical simulation of the barotropic tides in the
- Tunisian shelf and the Strait of sicily. J. Mar. Syst. 63, 162–182.
- Barkan, R., Winters, K. B., & McWilliams, J. C. (2017). Stimulated imbalance and the enhancement of eddy kinetic energy
- dissipation by internal waves. Journal of Physical Oceanography, 47, 181–198. https://doi.org/10.1175/jpo-d-16-0117.1
- Barkan, R., Srinivasan, K., Yang, L., McWilliams, J. C., Gula, J., & Vic, C. (2021). Oceanic mesoscale eddy depletion
- catalyzed by internal waves, Geophysical Research Letters, 48, e2021GL094376, https://doi.org/10.1029/2021GL094376
- 515 Bel Hassen, M., Hamza, A., Zouari, A., Drira, Z., Akrout, F., and Messaoudi, S. (2010). Temporal and seasonal scale
- variations of phytoplankton biomass control in the Gulf of Gabes. Vie et Milieu, 60(1), 17-26.
- Ben Ismail, S., Sammari, C., Béranger, K., and Lellouche, P. (2010). Atlas des données hydro-logiques des côtes
- tunisiennes. Institut National des Sciences et Technologies de la Mer 169 pp.
- 519 Ben Ismail, S., Sammari, C., and Béranger, K. (2015). Surface Circulation Features along the
- 520 Tunisian Coast: Central Mediterranean Sea. 26 the IUGG General Assembly, Prague. Czech Republic June 22 July 2.
- 521 Ben Ismail S, Costa E, Jaziri H, Morgana S, Boukthir M, Ben Ismail MA, Minetti R, Montarsolo A, Narizzano R, Sammari
- 522 C, Faimali M and Garaventa F (2022) Evolution of the Distribution and Dynamic of Microplastic in Water and Biota: A
- 523 Study Case From the Gulf of Gabes (Southern Mediterranean Sea). Front. Mar. Sci. 9:786026. doi:
- 524 10.3389/fmars.2022.786026
- 525 Blazevski, D., and Haller, G. (2014). Hyperbolic and elliptic transport barriers in three-dimensional unsteady flows. Physica
- 526 D, 273, 46–62.

- 527 Bouzaiene M., Menna M., Poulain P-M., Bussani A., and Elhmaidi D. (2020). Analysis of the Surface Dispersion in the
- 528 Mediterranean Sub-Basins. Front. Mar. Sci. 7:486.doi: 10.3389/fmars.2020.00486
- 529 Bouzaiene, M., Menna, M., Poulain, P.-M., and Elhmaidi, D. (2018). Lagrangian dispersion characteristics in the Western
- 530 Mediterranean. J. Mar. Res. 76, 139–161.
- Bouzaiene, M., Menna, M., Elhmaidi, D., Dilmahamod, A-F., and Poulain, P-M. (2021). Spreading of Lagrangian Particles
- in the Black Sea: A Comparison between Drifters and a High-Resolution Ocean Model, Remote Sensing 13, no. 13: 2603.
- 533 https://doi.org/10.3390/rs13132603
- Bower, A. S. (1991). A simple kinematic mechanism for mixing fluid parcels across a meandering jet. Journal of Physical
- 535 Oceanography, 21(1), 173–180.
- 536 Clementi, E., Pistoia, J., Delrosso, D., Mattia, G., Fratianni, C., Storto, A., et al. (2017a). A 1/24 degree resolution
- Mediterranean analysis and forecast modelling system for the Copernicus Marine Environment Monitoring Service.
- Extended abstract to the 8th EuroGOOS Conference, Bergen.
- 539 Clementi, E., Drudi, M., Aydogdu, A., Moulin, A., Grandi, A., Mariani, A, et al. (2023). Mediterranean Sea Physical
- Analysis and Forecast (CMS MED-Physics, EAS8 system) (Version 1) [Data set]. Copernicus Marine Service (CMS).
- 541 https://doi.org/10.25423/CMCC/MEDSEA ANALYSISFORECAST PHY 006 013 EAS8
- 542 Corti G., Cuffaro M., Doglioni C., Innocenti F., and Manetti P. (2006). Coexisting geodynamic processes in the Sicily
- 543 Channel. In: Y. Dilek & S. Pavlides (Eds), Postcollisional tectonics and magmatism in the Mediterranean region and
- 544 Asia. Geol. Soc. Am. Spec. Paper, 409: 83-96.
- Du Toit, P. C. (2010). Transport and separatrices in time-dependent flows (PhD thesis). Pasadena, CA: California Institute of
- 546 Technology. Retrieved from http://resolver.caltech.edu/CaltechTHESIS:10072009-165901284
- Elhmaidi, D., Provenzale, A., and Babiano, A. (1993). Elementary topology of the two-dimensional turbulence from a
- Lagrangian view-point and single particle dispersion. J. Fluid Mech., 257, 533–558
- 549 European Union-Copernicus Marine Service. (2021). EUROPEAN SEAS GRIDDED L4 SEA SURFACE HEIGHTS AND
- 550 DERIVED VARIABLES REPROCESSED (1993-ONGOING) [dataset]. Mercator Ocean International.
- 551 https://doi.org/10.48670/MOI-00141
- 552 European Union-Copernicus Marine Service. (2022). Mediterranean Sea, Bio-Geo-Chemical, L4, monthlymeans,
- dailygapfree and climatology Satellite Observations (1997-ongoing) [dataset]. Mercator Ocean International.
- 554 https://doi.org/10.48670/MOI-00300
- Escudier R, Clementi E, Cipollone A, Pistoia J, Drudi M, Grandi A, Lyubartsev V, Lecci R, Aydogdu A, Delrosso D, Omar
- M, Masina S,Coppini G and Pinardi N (2021) A High Resolution Reanalysis for the Mediterranean Sea. Front. Earth Sci.
- 9:702285 doi: 10.3389/feart.2021.702285
- Farazmand, M., and Haller, G. (2012). Computing Lagrangian coherent structures from their variational theory. Chaos: An
- Interdisciplinary Journal of Nonlinear Science, 22(1)
- Haller, G. (2002). Lagrangian coherent structures from approximate velocity data. Physics of Fluids, 14(6)

- Haller, G. (2015). Lagrangian Coherent Structures. Annual Review of Fluid Mechanics, 47(1)
- Hernández-García, E., Bettencourt, J., Garcon, V. Lopez, C., Rossi, V., Sudre, J., et al. (2010). Biological Impact of Ocean
- 563 Transport: A Finite-Size Lyapunov Characterization. 10.13140/2.1.4392.7048.
- 564 IOC. (1985). Manual on Sea Level Measurement and Interpretation. Inter governmental Oceanographic Commission,
- Manuals and Guides, 14, vol. I. Basic procedures, p. 75. Available online at:
- https://www.psmsl.org/train\_and\_info/training/manuals/.
- Jouini, M., Béranger, K., Arsouze, T.J., Beuvier, S., Thiria, M., Crepon, I., and Taupier-Letage, I. (2016). The Sicily
- 568 Channel surface circulation revisited using a neural clustering analysis of a high-resolution simulation. J. Geophys. Res.
- 569 Ocean. 121, 4545–4567.
- Kotta, D., and Kitsiou, D. (2019). Chlorophyll in the Eastern Mediterranean Sea: Correlations with Environmental Factors
- and Trends. Environments, 6, 98. https://doi.org/10.3390/environments6080098
- Liu, Y., Wilson, C., Green, M. A., and Hughes, C. W. (2018). Gulf Stream transport and mixing processes via coherent
- structure dynamics. Journal of Geophysical Research: Oceans, 123, 3014–3037. https://doi.org/10.1002/2017JC013390
- Macias, D., Garcia-Gorriz, E. and Stips, A. (2018), Major fertilization sources and mechanisms for Mediterranean Sea
- coastal ecosystems. Limnol. Oceanogr., 63: 897-914. https://doi.org/10.1002/lno.10677
- Marullo, S., Serva, F., Iacono, R., Napolitano, E., di Sarra, A., Meloni, D. (2023). Record-breaking persistence of the
- 577 2022/23 marine heat wave in the Mediterranean Sea. Environ. Res. Lett. 18 114041
- 578 10.1088/1748-9326/ad02ae
- Menna, M., Poulain, P.-M., Ciani, D., Doglioli, A., Notarstefano, G., Gerin, et al. (2019). New Insights of the Sicily Channel
- and Southern Tyrrhenian Sea Variability, Water, 11, 1355, https://doi.org/10.3390/w11071355
- Meyerjürgens, J., Ricker, M., Schakau, V., Badewien, T. H., & Staney, E. V. (2020). Relative dispersion of surfacedrifters in
- the North Sea: The effect oftides on mesoscale diffusivity. Journal of Geophysical Research: Oceans, 125,e2019JC015925.
- 583 https://doi.org/10.1029/2019JC01592
- Millot, C., and Taupier-Letage, I. (2005). Circulation in the Mediterranean Sea. In: Saliot, A. (eds) The Mediterranean Sea.
- Handbook of Environmental Chemistry, vol 5K. Springer, Berlin, Heidelberg. https://doi.org/10.1007/b107143
- Morales-Márquez, V., Hernández-Carrasco, I., Fox-Kemper, B., and Orfila, A. (2023). Ageostrophic contribution by the
- 587 wind and waves induced flow to the lateral stirring in the Mediterranean Sea. Journal of Geophysical Research: Oceans,
- 588 128, e2022JC019135. https://doi. org/10.1029/2022JC019135
- Okubo, A. (1970). Horizontal dispersion of floating particles in the vicinity of velocity singularities such as convergence.
- 590 Deep Sea Res. Oceanogr. Abstr., 17, 445–454.
- 591 Onu, K., Huhn, F., and Haller, G. (2015). LCS Tool: A computational platform for Lagrangian coherent structures, Journal
- 592 of Computational Science, Volume 7, Pages 26-36, ISSN 1877-7503, https://doi.org/10.1016/j.jocs.2014.12.002.
- 593 Othmani, A., Béjaoui, B., Chevalier, C., Elhmaidi, D., Devenon, J.L., and Aleya, L. (2017). High-
- resolution numerical modelling of the barotropic tides in the Gulf of Gabes, eastern Mediterranean Sea (Tunisia). J. Afr.

- 595 Earth Sci. 129, 224–232
- 596 Pinardi, N., Zavatarelli M., Adani M., Coppini G. Fratianni C., Oddo P., et al. (2015), Mediterranean Sea large-scale low-
- frequency ocean variability and water mass formation rates from 1987 to 2007: A retrospective analysis, Progress in
- 598 Oceanography, Volume 132, Pages 318-332, ISSN 0079-6611, https://doi.org/10.1016/j.pocean.2013.11.003.
- Poulain, P.M., and Zambianchi, E. (2007). Surface circulation in the central Mediterranean Sea as deduced from Lagrangian
- drifters in the 1990s. Cont. Shelf Res. 27, 981–1001.
- Poulain, P.-M. (1993). Estimates of horizontal divergence and vertical velocity in the equatorial Pacific. J. Phys. Oceanogr.,
- 602 23, 601–607.
- Poulain, P.-M., Centurioni, L., Brandini, C., Taddei, S., Berta, M., and Menna, M.: Relative dispersion and kinematic
- properties of the coastal submesoscale circulation in the southeastern Ligurian Sea, Ocean Sci., 19, 1617–1631,
- 605 https://doi.org/10.5194/os-19-1617-2023, 2023.
- Poulain, P.-M., Menna, M., and Mauri, E. (2012b). Surface geostrophic circulation of the Mediterranean Sea derived from
- drifter and satellite altimeter data. J. Phys. Oceanogr. 42, 973–990. doi: 10.1175/JPO-D-11-0159.1
- Rossi, V., Lopez, C., Sudre, J., Hernández-García, E., Garçon, V. (2008). Comparative study of mixing and biological
- activity of the Benguela and Canary upwelling systems. Geophysical Research Letters, 35 (11), pp.L11602.
- 610 ff10.1029/2008GL033610ff. ffhal-02296657
- Rühs, S., van den Bremer, T., Clementi, E., Denes, M. C., Moulin, A., and van Sebille, E.: Non-negligible impact of Stokes
- drift and wave-driven Eulerian currents on simulated surface particle dispersal in the Mediterranean Sea, Ocean Sci., 21,
- 613 217–240, https://doi.org/10.5194/os-21-217-2025, 2025.
- Rypina, I. I., Pratt, L. J., and Lozier, M. S. (2011). Near-surface transport pathways in the North Atlantic Ocean: Looking for
- through put from the subtropical to the subpolar gyre. Journal of Physical Oceanography, 41(5), 911–925.
- 616 Salgado-Hernanz, P.M., Racault, M.-F., Font-Muñoz, J.S., Basterretxea, G. (2019). Trends in phytoplankton phenology in
- the Mediterranean Sea based on ocean-colour remote sensing, Remote Sensing of Environment, Volume 221, Pages 50-
- 618 64, ISSN 0034-4257, https://doi.org/10.1016/j.rse.2018.10.036
- 619 Sahnoun, W-F., Njah, H., Hamza, A., Barraj, N., Mahfoudi, M., Rebai, A., et al. (2017). Using general linear model,
- 620 Bayesian Networks and Naive Bayes classifier for prediction of Kareniaselliformis occurrences and blooms, Ecological
- 621 Informatics, Volume 43, 2018, Pages 12-23, ISSN 1574-9541, https://doi.org/10.1016/j.ecoinf.2017.10.017.
- Shadden, S-C., Lekien, F., Marsden, J-E. (2005). Definition and properties of Lagrangian coherent structures from finite-
- time Lyapunov exponents in two-dimensional a periodic flows. Physica D: Nonlinear Phenomena, 212(3-4)
- Song, D., Wang, X. H., Kiss, A. E., and Bao, X. (2011). The contribution to tidal asymmetry by different combinations of
- tidal constituents, J.Geophys. Res., 116, C12007, doi:10.1029/2011JC007270
- 626 Sammari, C., Koutitonsky, V., and Moussa, M. (2006). Sea level variability and tidal resonance in the Gulf of Gabes.
- 627 Tunisia. Cont. Shelf Res. 26, 338–350.
- Sammari, C., Millot, C., Taupier, Letage, I., Stefani, A., Brahim, M. (1999). Hydrological characteristics in the Tunisia-

- Sardinia-Sicily area during spring 1995. Deep-Sea Res. I46, 1671–1703
- 630 Sorgente, R., Olita, A., Oddo, P., Fazioli, L., and Ribotti, A. (2011). Numerical simulation and decomposition of kinetic
- energy in the Central Mediterranean: insight on mesoscale circulation and energy conversion. Ocean. Sci. 7, 503–519.
- Siegelman, L., 2020: Energetic Submesoscale Dynamics in the Ocean Interior. J. Phys. Oceanogr., 50, 727–749,
- https://doi.org/10.1175/JPO-D-19-0253.1.
- Suthers, I.M., Schaeffer, A., Archer, M., Roughan, M., Griffin, D.A., Chapman, C.C., Sloyan, B.M. and Everett, J.D. (2023),
- Frontal eddies provide an oceanographic triad for favorable larval fish habitat. Limnol Oceanogr, 68: 1019-1036.
- https://doi.org/10.1002/lno.12326

- Taburet, G., Sanchez-Roman, A., Ballarotta, M., Pujol, M., Legeais, J., Fournier, et al. (2019). Duacs dt2018: 25 years of
- reprocessed sea level altimetry products. Ocean Science, 15, 1207–1224.
- Vigo, I., Sempere, M., Chao, B., and Trottini, M., (2018). Mediterranean Surface Geostrophic Circulation from Satellite
- Gravity and Altimetry Observations. Pure and Applied Geophysics. 175. 10.1007/s00024-018-1911-0.
- Vigo, M.I., García-García, D., Sempere, M.D., and Chao, B.F. (2018b). 3D Geostrophy and Volume Transport in the
- 642 Southern Ocean. Remote Sens. 10, 715. https://doi.org/10.3390/rs10050715
- Weiss, J. (1991). The dynamics of the enstrophy transfer in two dimensional turbulence. Phys. D, 48, 273–294.
- Zayen, A., Sayadi, S., Chevalier, C., Boukthir, M., Ben Ismail, S., and Tedetti, M. (2020). Microplastics in surface waters of
- the Gulf of Gabes, southern Mediterranean Sea: distribution, composition and influence of hydrodynamics. Estuar. Coast.
- 646 Shelf Sci. 242:106832. doi: 10.1016/j.ecss.2020.106832